THE Journal OF THE AMERICAN LEATHER CHEMISTS ASSOCIATION

June 2024 Vol. CXIX, No.6 *JALCA* 119(6), 245–292, 2024

119th Annual Convention

TO BE ANNOUNCED

For more information go to:
leatherchemists.org/annual_convention.asp

Contents

Distributed by
University of CINCINNATI
LIBRARY PUBLISHING SERVICES

An imprint of the University of Cincinnati Press

ISSN: 0002-9726

Communications for Journal Publication

Manuscripts, Technical Notes and Trade News Releases should contact:
Mr. Steven D. Lange, Journal Editor, c/o University of Cincinnati, 5997 Center Hill Ave., Bldg. C, Cincinnati, OH 45224, USA
E-mail: jalcaeditor@gmail.com Mobile phone: (814) 414-5689

Contributors should consult the Journal Publication Policy at:
http://www.leatherchemists.org/journal_publication_policy.asp

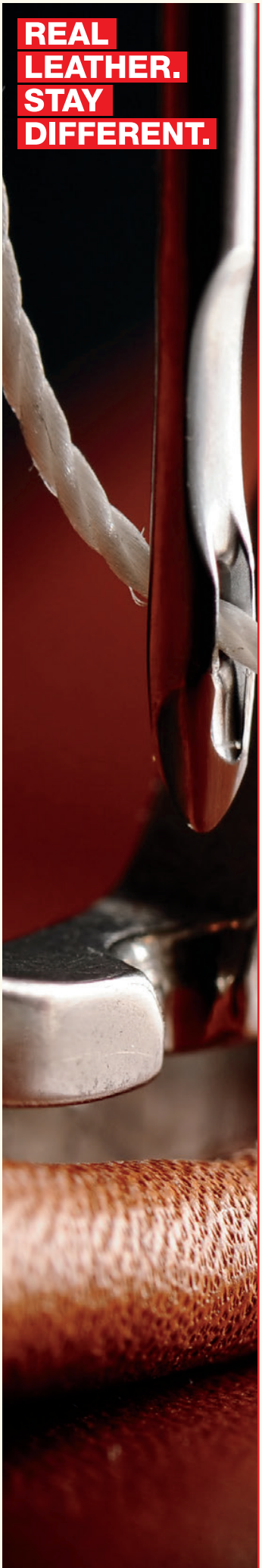

LEATHER BY NUMBERS:

FACTS AND FIGURES FROM THE US LEATHER INDUSTRY AND BEYOND

Note: All figures as of January 2021 or latest available.

ZERO cattle are killed to make US leather. US hides have been valued at JUST 1-2% of a cow's total value for the last two years, which is why they are considered a by-product and often end up as waste. The average price per head of US cattle is $2,000-2.200, while hides vary in price from $5 TO $35 PER PIECE, if sold at all. (1)

330M hides come from the meat and dairy industries around the world. Approximately 34M were processed the US. (2) AS MANY AS 2.4M US HIDES ended up as landfill in 2019, this is 7% of the national total.

Worldwide the waste figure is approximately 40% or 132M hides. With the average hide weighing 25Kg this means that 3M TONNES are thrown away ever year.

Leather production turns more than 4.5M TONNES OF potential waste, every year, into usable, durable goods. This saves 2.7M TONS OF GREENHOUSE GAS EMISSIONS from landfill sites. (3)

Production, processing and distribution of hides and leather products directly employs an estimated 5,486 individuals, who collectively earn more than $384M. US exports of hides and leather was over $1.5BILLION in 2021. (4)

The US exports approximately 95% of all cattle hide and wet blue leather products it produces, worth $2.85BILLION. (5)

Around 45% of global leather production is used to make footwear, 22% for clothing, bags and accessories, 18% for car upholstery, and about 15% for furniture. (6)

Water consumption for the production of leather from cattle hides has fallen by more than 35% in the past 25 years, down from 60 CUBIC-METERS per ton of hides to 38 CUBIC-METERS per ton. US tanneries are required, by law, to connect to effluent treatment plants to prevent pollution. (7)

Leather will biodegrade in LESS THAN 50 YEARS. In contrast, it can take 500 YEARS or more for synthetics, made from petrochemicals, to degrade. (8)

ReFed's conversion rate for food waste is for EACH METRIC TON OF WASTE DISPOSAL there is 9.87MT of CO2 EQUIVALENT emitted. In this case, mostly as methane. (9)

This factsheet is produced by the Leather and Hide Council of America (L&HCA), established to promote the US leather industry which is responsible for a significant proportion of the international trade in hides. The L&HCA works to establish best practice in US leather production and to share this worldwide. Figures quoted refer to the USA unless otherwise stated.

SOURCE:

(1) https://downloads.usda.library.cornell.edu/usda-esmis/files/rx913p88g/w0893q25p/5d86qb66f/lstk0223.pdf
(2) https://downloads.usda.library.cornell.edu/usda-esmis/files/r207tp32d/pg15cj85z/hd76t466z/lsan0422.pdf
(3) 2020 LHCA Infographic
(4) John Dunham & Associates, Economic Impact of the Meat Industry (2016)
(5) https://thesustainabilityalliance.us/wp-content/uploads/2020/04/US-Hide-Skin-and-Leather-Factsheet-0420.pdf
(6) TBC
(7) 2020 LHCA factsheet
(8) https://en.wikipedia.org/wiki/Leather#:~:text=Leather%20biodegrades%20slowly%E2%80%94taking%2025,or%20more%20years%20to%20decompose
(9) https://insights-engine.refed.org/impact-calculator?inputs=%7B%22sector%22%3A%22manufacturing%22%2C%22type%22%3A%22fresh-meat-seafood%22%2C%22unit%22%3A%22tons%22%2C%22alternative%22%3Afalse%2C%22destinations%22%3A%5B%7B%22key%22%3A%22refuse-discards%22%2C%22current%22%3A1%7D%5D%7D

JOURNAL OF THE
AMERICAN LEATHER CHEMISTS ASSOCIATION

Proceedings, Reports, Notices, and News
of the
AMERICAN LEATHER CHEMISTS ASSOCIATION

THE JOURNAL OF THE AMERICAN LEATHER CHEMISTS ASSOCIATION (USPS #019-334) is published monthly by The American Leather Chemists Association, c/o University of Cincinnati, 5997 Center Hill Ave., Bldg. C, Cincinnati, Ohio 45224. Telephone (513) 290-2505. Single copy price: $10.00 members, $20.00 non-member plus shipping and handling. Subscriptions: $185 for hard copy plus postage and handling of $60 for domestic subscribers and $70 for foreign subscribers; $220 for ezine only; and $240 for hard copy and ezine plus postage and handling of $60 for domestic subscribers and $70 for foreign subscribers.

Periodical Postage paid at Cincinnati, Ohio and additional mailing offices. Postmaster send change of addresses to The American Leather Chemists Association, c/o University of Cincinnati, 5997 Center Hill Ave., Bldg. C, Cincinnati, Ohio 45224.

Website: www.leatherchemists.org E-mail: hallks@ucmail.uc.edu

Member of
italtannery.com

The new standard is here

ITALTANNERY Project

ALL THE QUALITY YOU NEED

MADE EASY

RELIABILITY | CONTROL | HIGH TECHNOLOGY | SUSTAINABILITY

MILLING DRUMS

SPRAY BOOTHS

TUNNEL DRYERS

AUTOMATION

Erretre
Tannery Innovations

more

Via Ferraretta, 1 - 36071 Arzignano VI, Italy | +39 0444 478312 | info@erretre.com | **erretre.com**

Sky Fruit Seed Crush (SFSC): A Potential Source of less Salt Curing of Raw Goatskin

by

Md. Abdur Razzaq,[1]* M. Mahfujur Rahman,[2] Md. Motinur Rahman[2] and Md. Salamat Ullah[3]

[1]*Leather Research Institute, Bangladesh Council of Scientific and Industrial Research (BCSIR),* Dhaka, Bangladesh

[2]*Bangladesh Atomic Energy Commission (BAEC),* Dhaka, Bangladesh.

[3]*Institute of Leather Engineering and Technology, University of Dhaka*

Abstract

The curing of raw hides and skins using sodium chloride salt is a widely recognized technique, although it has negative consequences for the environment by elevating water salinity and introducing a significant amount of Total Dissolved Solids (TDS). In order to tackle this issue, goat skin was conserved through the utilization of a mixture consisting of crushed sky fruit seeds and sodium chloride salt. Various ratios of mixtures were applied to raw goat skin to determine an optimal outcome. The most favorable result was achieved by utilizing a blend of 10% seed crush and 10% salt, based on the weight of the raw skin. A control specimen was run with the experimental specimen, and preservation-related variables such as odor, hair loss, shrinkage temperature, moisture level, and bacterial population were evaluated. After preservation, the experimental sample and a control sample were subjected to the standard leather processing technique. The liquor from both samples was analyzed to confirm the impact of the environment on preservation. The experimental trial indicated a 59% decrease in total dissolved solids (TDS) and a 44% reduction in chloride (Cl–) content. The processed leather samples were assessed for their quality through an analysis of their physical properties. Besides, the fiber structures were assessed using a scanning electron microscope (SEM). The comparative evaluation of the physiochemical properties of the introduced preservation showed superb results with the hope of new preservation possibilities.

Introduction

Preservation or curing is the primary stage of leather processing where an appropriate conservation technique is followed within 5–6 h after the death of the animal or flaying the skin to desist putrefaction.[1] Amongst dozens of preservation methods commonly practiced techniques are salting, drying, cooling and chilling.[2] Salting is the most popular leather conservation method which includes application of 40-50% common salt (based on the green weight of skin) on fresh hides and skins.[3] Since, approximately 13–17% salt is fixed into the hide and skins, the excess unabsorbed salts are disposed into nearby rivers in form of waste water during de-salting and soaking operations in tanneries.[4] This provides the initial pollutants to the aquatic ecosystem and includes addition of excessive amount of chlorides, sulfides and TDS.[5] Consequently, immense degradation of water occurs which severely affects the aquatic life and enters into the human food chain.[6] Besides, an adverse effect on crop production appears due to deterioration of soil fertility.[7] In addition to that, there is extreme possibility of blending of chlorides with deeper groundwater which will result in adverse phenomenon for human civilization.[8]

Hence, there is a strong appeal among scientific communities to introduce environment friendly leather preservation recipes. Traditional leather conservation techniques were based on physical treatments or application of any substance on leather with a view to either destruct bacteria or prevent bacterial action.[9] Phyto-based organic preserving agents are abundantly available and a potential source of diminishing pollution load occurring in leather soaking.[10] A noticeable aptitude of phyto-based techniques to preserve raw hides and skins has been proposed in recent scientific articles. Diverse parts of plant viz. leaf paste of *Acalypha indica,*[11] dry leaf powder of *Calotropis gigantean,*[12] seed oils[13] and peels etc. has been being introduced by researchers in this regard.

Swietenia macrophylla, is a locally available timber tree and commonly known as mahogany tree.[14] Although native to the West Indies, it has been expanded in southern Asia (India, Sri Lanka, Bangladesh) and in the pacific (Malaysia, Philippines, Indonesia and Fiji), and West Africa by plantation.[15] Mahogany roots, barks, seeds etc. have been used for the treatment of hypertension, diabetes, malaria, amoebiasis, coughs, chest pain and tuberculosis, and as an abortifacient, antiseptic, astringent, depurative, and tonic.[16] A recent study mentioned the potentiality of sky fruit seed extract as a tanning agent in the leather industry.[17]

The synthesis of modified triterpenes known as limonoids, which contain a 4,4,8-trimethyl-17-furanyl steroid skeleton, distinguishes the mahogany (Meliaceae) family.[18]

Presence of triterpenoids in mahogany family is an important constitutive and defensive substance against microbes.[19] The antimicrobial properties of different parts of Swietenia Mahogany has been reported in many research articles.[20,21] Dye extracted

*Corresponding author email: arazzaq-lri@bcsir.gov.bd

Manuscript received January 1, 2024, accepted for publication February 3, 2024.

from sky fruit seed pods has exhibited antimicrobial efficacy.[22,23] Mahogany seed oil has applications in both agriculture to control pests and leather preservation.[18]

Realizing potentiality, Swietenia Mahogany seed extract was applied to raw goat skin with a view to develop a salt free skin preservation technique.[18] In this research, powdered form of *Swietenia macrophylla* fruit, also named as Sky Fruit, has been utilized in association with minimum amount of salt to preserve raw goat skin. The goal of this study was to develop a low salt preservation technique with a view to decrease environmental pollution during skin preservation.

Material and Methods

2.1 Collection of Skin and chemicals

After purchasing freshly flayed goat skin samples from a local trader, the samples were washed in water to remove impurities such as dirt, filth, blood, and other substances. After that, the skin was hung for a few minutes so that the water could drain off. Tannery Estate in Savar, Dhaka was the source of all of the utilized chemicals and auxiliaries, all of which were of a commercial grade and purchased there. For the determination of the biochemical and pollution index, chemicals of analytical grade were utilized.

2.2 Preparation of SFSC

The Sky fruits were gathered from the Plantation region of the Leather Research Institute, and once the pods were opened, the fruits were found inside. After the seeds had been peeled, they were left out in the sun for two full days to dry. After that, the seeds were ground into a fine powder with an analytical grinder and stored at room temperature.

2.3 FTIR Analysis

To find out the functional groups of the SFSC, a Perkin-Elmer FTIR spectrophotometer with UATR was employed. The obtained absorbance from the FT-IR Spectra of the samples was recorded and studied according to the literature.[24,25] The stored powder was directly placed on a ZnSe-diamond crystal of the FTIR which enables the acquisition of FTIR spectra directly from a sample without the need for additional sample preparation.[26]

2.4 Application of SFSC for Curing

During our preliminary lab assessment, variable twelve (12) ratios (w/w) of SFSC and salt mixture were applied on several portions of freshly flayed goat skins as shown in Table I to determine the optimum proportion for the preservation during initial trial for about 30 days.

All measurement were taken based on the weight of raw skin. Organoleptic properties viz. odor, hair slip, and moisture content of all the samples were assessed periodically. All samples were kept in the same environmental conditions. The preservation parameters viz. moisture content (%), bacterial count, hair slip, odor, shrinkage temperature and extractable nitrogen were assessed periodically (raw, 1st, 4th, 7th, 15th and 30th days of preservation. Desired combination was identified on the evaluation of preliminarily preserved goat skins. The salt and SFSC utilized during determination of Organoleptic properties viz. Hair slip, odor and physical feel have been illustrated for a full observation period of 30 days in the Table I. Among the twelve preserved samples one sample with supreme performance was selected for final trial. During the final assessment, a single section of recently removed goat hide was acquired. One side of the setup was designated for the experimental group, while the other side was designated for the control group.

Figure 1. Sky fruit tree with fruit, peeled seeds and crushed seed powder

Table I

Percentage of salt and SFSC used for preliminary trials

Sample ID	A	B	C	D	E	F	G	H	I	J	K	L
Salt (%)	50	0	25	20	15	10	5	10	15	20	25	12.5
SFSC (%)	0	18	10	10	10	10	10	5	5	5	5	7.5

2.5 Moisture Content

During days of assessment, small pieces (1-2g) of skin samples were cut and placed on the sample pan to determine moisture content by using a High-performance Moisture Analyzer model WBA-110M.

2.6 Nitrogen Content

To quantify total extractable nitrogen, 5g sample from the preserved skins were taken and treated with ten times (w/v) its weight of distilled water into a conical flask. The flask was shaken at 200 rpm for 30 minutes by keeping it on a shaker. Then the liquor was filtered using filter paper and subjected to the digestion unit of kjeldhal chamber controlling temperature 400°C. The sample was then distilled over into a receiving flask containing 50ml sodium hydroxide solution in the distillation chamber. Finally the nitrogen content was determined following titration method described in the literature.[27]

2.7 Bacterial Count

Skin samples of known weight (5g) were cut and processed through the nitrogen content determination procedure up to filtration at various stages of preservation. One milliliter of the filtrate was taken and diluted with sterile water to make 10 mL. The solution was thoroughly shaken to obtain identical bacteria suspension, and 0.1 ml was placed in a sterile petri plate. The sample was serially diluted up to the required colony formation level. Molten nutrient agar was added and carefully shaken to ensure that bacteria were distributed uniformly. Finally, petri plates were placed in an incubator for 48 hours at 37°C.[28] A bacterial colony counter (Bioevopeak CC-J2) was used to count the bacterial population.

2.8 Hydrothermal Property

Shrinkage temperature indicates the hydrothermal property of hides and skins. It was determined by using SATRA TD 114 shrinkage temperature tester. Test samples (80×10 mm) were cut and hooked in the holder of shrinkage temperature apparatus which was then dipped in a bath containing a glycerin/water solution in the ratio of 70:30. The rate of temperature increment was 3°C/min. The skin's shrinkage temperature was recorded as the temperature at which the shrinkage began.

2.9 Leather Making

After finishing continuous observation of the preserved skin whose duration was 30 days, both the preserved samples were processed up to crust leather by following conventional leather processing technique.

2.10 Pollution Load Analysis

The wastewater in soaking operation generated from the control as well as experimental trials were collected and analyzed for Biochemical Oxygen Demand (BOD), Chemical Oxygen Demand (COD), Total Dissolved Solids (TDS) and Chloride (Cl) content. The standard APHA methods were followed in analysis and all the experiments were triplicated.[29]

2.11 Physical Properties Analysis

The prepared crust leathers were left about 1 month for aging. Physical strength of the leathers was determined after conditioning at temperature 23±2°C and relative humidity 50±2% for defined hours relevant to method. Then the samples were taken from the specified sampling location. The properties such as the tensile strength, elongation at break, tear strength, and bursting strength were assessed following SATRA TM 43, TM 162, and TM 24 respectively.

2.12 SEM Analysis

Processed wet blue leathers from the experimental and control trials were subjected to an Electron Microscope (VEGA3 TESCAN, Czech Republic) for evaluating their morphological characteristics. The fiber structures were assessed by enabling cross section of the leather and by accelerating voltage 30.0 kV with magnification 500X.

Results and Discussions

3.1 FTIR analysis result of SFSC

FTIR spectroscopy can identify unknown substances, analyze chemical composition, study molecular structure, monitor chemical reactions, and investigate materials' physical properties. Pharmaceuticals, polymers, forensics, environmental science and more use it.[30] FTIR peak of the SFSC has been labeled and depicted at the Figure 3. As seen in the figure, the Fourier transforms infrared (FT-IR) spectrum analysis result shows various functional groups.

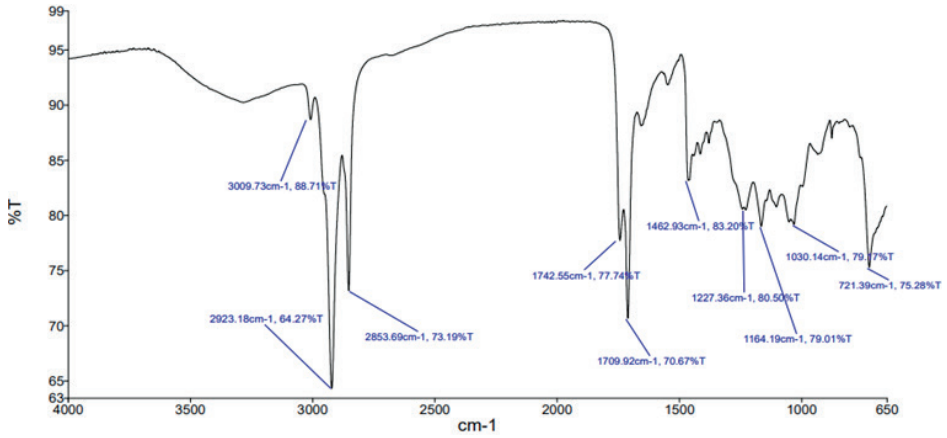

Figure 3. FTIR Spectrum of mahogany seed crush.

Table II

Organoleptic properties of goat skin preserved in preliminary trial

Sample ID	A	B	C	D	E	F	G	H	I	J	K	L
Odor	No	No	No	No	No	No	No	Yes	No	No	No	No
Hair slip	No	No	No	No	No	No	Yes	Yes	Yes	No	No	No
Physical Feel	Soft	Hard	Soft	Soft	Soft	Soft	Soft	Soft	Soft	Medium Soft	Soft	Medium hard

The occurrence of aromatic rings in flavonoids results in absorption peaks at approximately 3009 cm^{-1}, signifies the stretching of C-H bonds within the aromatic rings. Peak at 2923.18 cm^{-1} and 2853.69 cm^{-1} shows the presence of aliphatic groups. The absorption peak at 1742.55 cm^{-1} in the flavonoid structure corresponds to the stretching of the carbonyl group (C=O), specifically indicating C=O stretching.

The absorption peak at 1742.55 cm^{-1} in the flavonoid structure demonstrated the inhibitory effects of flavonoids on the proliferation and maturation of fungal pathogens. Presence of ester group at the wavelength 1709.92 cm^{-1} is for presence of fatty acid. Hence, it can be concluded that the SFSC could show strong antimicrobial effect on preservation.

3.2 Organoleptic Properties

The initial indication of putrefaction comes about during the protein degradation process carried out by bacteria in the hair bulb during the early stages of decomposition.[31] Therefore, it is commonly accepted that odor emission and hair slip are important factors to consider when evaluating the effectiveness of a curing method, as they can serve as indicators of the beginning stages of the putrefaction process.

Figure 2. Skins Preserved with 10% NaCl+10% SFSC (Experimental trial) and 50% NaCl (Control trial).

Table II describes the properties of preserved leather during the preliminary trial of a full month. Sample A was for conventional control trial and exhibited no change in result as estimated. For sample B, 18% SFSC was applied, and it was found hard after the preservation duration. Samples C, D, E and F had 10% SFSC and variable amounts of salt. There was neither existence of hair slip nor formation of hard skin for these combinations. Samples G, H and I had 5% SFSC and variable amounts of salt. The surfaces of these three tests showed signs of fungal growth, worms and hair loss, as well as a slight putrid odor. Samples J and L showed medium hard skin. Sample K has a combination of 25% salt and 5% SFSC. This combination was sustained in the trial. Although samples C, D, E, F and K showed brilliancy in preservation, the sample F consists of minimum amount of salt. Hence, considering minimum use of salt, we decided to proceed with the sample F for the final experimental trial holding combination of 10% salt and 10% SFSC.

3.3 Moisture Content

The durability, pliability, and aesthetic quality of leather goods depend on the leather's ability to withstand and be unaffected by moisture.[32] Fluctuation of moisture content of the experiment has been depicted on the Figure 4 where identical moisture content was observed for the fresh sample. After 1 day preservation duration, the moisture content of the experiment and control samples was found to be 54% and 57% respectively. The moisture content of the experimental trial decreases to 30% after a 30-day preservation period which is unfavorable for bacterial growth.

The moisture content of the control trial exhibits a gradual decline, ultimately reaching a value of 35%. In contrast, the moisture content of the experimental trial decreases to 30% after a 30-day preservation period. The SFSC caused slightly more dehydration compared to

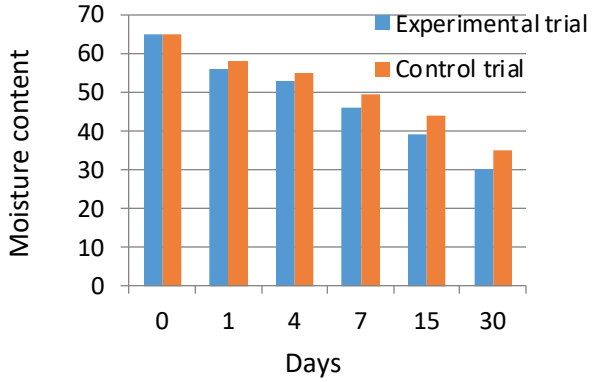

Figure 4. Moisture content of preserved skins.

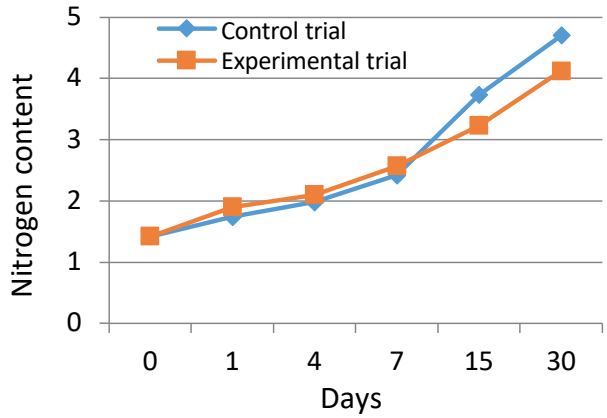

Figure 5. Nitrogen Content of preserved skins- lower value of the experimental preservative combination is in no risk of putrefaction.

the control trial. This might be due to tanning effect of the applied seed extract and evaporation by atmospheric action.[17,18] Moreover, comparatively lower moisture content of the preserved leather would facilitate minimizing transport cost as well as acceleration of antimicrobial activity.[13] The lower moisture content will also be helpful to inhibit bacterial growth on the preserved skin.[12]

3.4 Nitrogen Content

Bacterial decomposition of hides/skins produces extractable nitrogen.[33] The level of putrefaction caused by microorganisms can be determined by testing the hide or skin for extractable nitrogenous compounds. The total extractable nitrogen content of the experimental and control skins at varying times over a 30-day preservation period has been presented in the Figure 5. From the Figure it is evident that the content of extractable nitrogen for both trials was similar until the 7th day of preservation.

This might be due to the harmonious preservation of the skin. At the end of 30 days the experimental sample discharged comparatively less amount of extractable nitrogen. The extractable nitrogen value of both trials was very low and comparable with values of many with similar preservation techniques. Hence, it can be expressed that the experimental preservative combination is in no risk of putrefaction.

3.5 Bacterial Count

The deterioration status of hides and skins can be described by the number of bacterial colonies present on it at the time of preservation.[13] Table III presents the quantitative data on the bacterial colony count observed in the samples collected for monitoring and study purposes. The samples were obtained from fresh (raw) sources on the fresh, 1st, 4th, 7th, 15th, and 30th day of the experiment. In raw goat skin, the bacterial population was about 3×10^8 CFU/g. The results revealed that the quantity of bacteria present in the experimental sample is comparatively lower than the control sample; both during the initial and final stages.

3.6 Shrinkage Temperature

Shrinkage temperature serves as a barometer for any structural alterations in the skin matrix because putrefaction causes collagen to become less stable.[34] The shrinkage temperature is a quantitative assessment of the degradation of stabilizing linkages present within the collagen matrix.[35] Shrinkage temperature variations of both trials are depicted at the Figure 6. The initial shrinkage temperature was 66°C. The shrinkage temperature value of the experimental trial was determined to be 68.50°C after a 30-day preservation period. In a similar manner, the control trial exhibited consistent results and ultimately reached a temperature of 67.70°C on the 30th day.

Table III

Bacterial Count in the preserved skins observed

Days	Experimental (CFU/g)	Control (CFU/g)
0	3×10^8	3×10^8
1	5.5×10^7	4×10^8
4	4×10^7	6.2×10^7
7	4.5×10^6	5×10^7
15	7×10^5	3.7×10^7
30	3.1×10^5	6.3×10^6

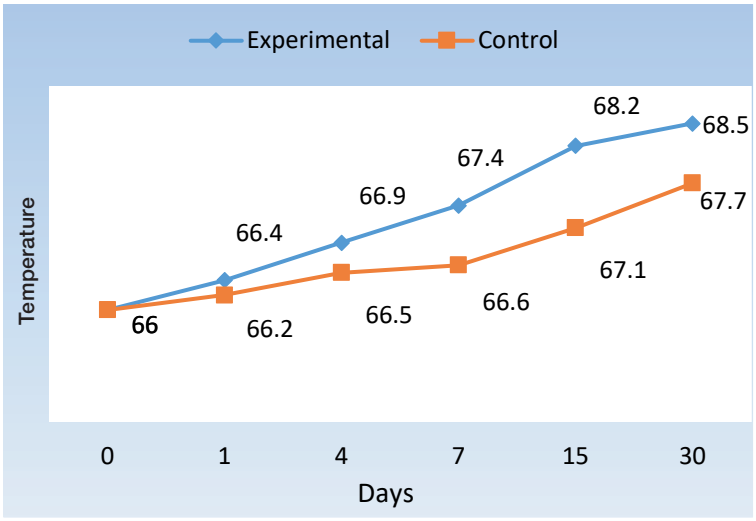

Figure 5. Shrinkage Temperature (°C) of preserved skins.

The observed increase in shrinkage temperature of the experimental trial was due to the partial tanning effect of SFSC. The thermal properties of collagen exhibit variability depending on the specific curing agents and processing conditions employed.[36] Therefore, it can be inferred that the developed curing system did not induce any adverse structural alterations in the skin matrix.

3.7 Pollution load Analysis

To assess environmental effect of the experimental preservation, soak liquor was allowed to undergo few test parameters and has been illustrated in the Figure 4. The Figure displays the pollution load generated during the soaking process of the optimized experimental and corresponding control samples, including BOD, COD, TDS, and chlorides. There was a significant reduction in TDS and Chloride content. Since the 50% salt was used in the experimental trial, there was around 48% reduction in Chloride content. On the other hand, approximately 43% minimization of Total Dissolved Solid (TDS) was obtained in the experimental trial. Increased value of Total Suspended Solid (TSS) was found due to less solubility of the dried powders. Since plant materials contain biological substances, there was a slight decrease in BOD and COD values.[3]

3.8 Physical properties study

The tabulated physical properties in Table V indicate the physical strengths e.g., tensile strength, elongation at break, tear strength and grain crack of the experimental trial and the control trial. Values of both trials are much above the minimum requirement and comparable to each other. Hence, the SKFC preservation technique does not affect the physical properties of preserved skins.

Table VI

Pollution load analysis of soak liquor of preserved goat skin

Parameter	Experimental(g/L)	Control (g/L)	Reduction (%)
Total Dissolved Solid (TDS)	18±0.17	42±0.21	43
Total Suspended Solid (TSS)	26±0.10	8±0.53	
Chloride Content (Cl^-)	8±0.11	16.5±0.09	48
Biological Oxygen Demand (BOD)	1.3±0.08	1.4±0.07	
Chemical Oxygen Demand (COD)	4.5±0.06	4.7±0.06	

Table V

Physical properties of processed crust leather

Parameter	Experimental	Control	Standard requirement (ISO)
Tensile strength(kgf/cm^2)	285±7	290±7	200
Elongation at break (%)	50.6±5	47.8±5	30-40%
Tear strength(N)	43±6	46.2±6	30
Grain Crack Strength(N)	22.2±4	24.0±4	20

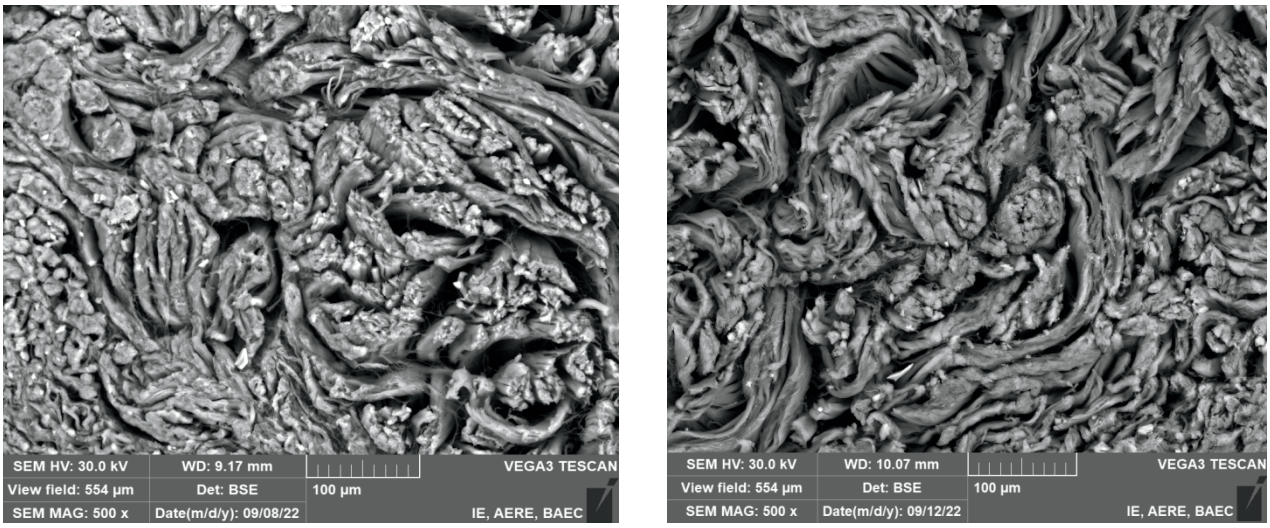

Figure 7. SEM images of processed wet blue goat skin showed no any significant change in the leather prepared from the experimental goat skin compared to the goat skin preserved with control trial.

3.9 SEM Analysis

High-resolution imaging, surface analysis, examination of fiber structure, cross-section analysis, defect detection, and comparative studies are all made possible by SEM, making it an indispensable tool for the study of leather's form.[37] SEM images of the leather processed crust leather from all trials have been illustrated in the Figure 7.

Conclusion

In pursuit of attaining sustainable industrialization, diligent researchers are tirelessly endeavoring to render each industrial operation ecologically sound. This study aimed to explore the potential of utilizing sky fruit seed crush (SFSC) in conjunction with conventional salt as a means to decrease the overall salt consumption. The FTIR study found presence of flavonoids, ester and fatty acids in the experimental substance which were indication of strong antimicrobial activities. Similar to other phyto-based preservation techniques, this preservation method necessitates the utilization of a 10% concentration of crushed sky fruit seeds and 10% concentration of sodium chloride and the evaluation of Bacterial colony counts found advantageous. The nitrogen content, moisture content, bacterial count, and shrinkage temperature properties of the leather preserved in the experiment were found to be satisfactory. The analysis of the immersed solution yielded remarkable findings. The preservation method demonstrated a significant impact on environmental pollution control, with the TDS accounting for 59% and salinity control accounting for 44% of the overall effectiveness. There was no statistically significant decrease observed in the levels of Biological Oxygen Demand (BOD) and Chemical Oxygen Demand (COD).

The scanning electron microscopy (SEM) analysis revealed that the fiber structure observed in the experimental trial was similar to that of the control trial. The strength properties under consideration include tensile strength, tearing strength, and the percentage of elongation exceeding the specified value as outlined in the International Organization for Standardization (ISO) guidelines. The novel preservation technique with reduced salt content exhibited exceptional performance. Furthermore, sky fruit exhibits extensive availability and presently lacks tangible economic worth. For a nominal charge, one can acquire the substance and employ a simple method of pulverization and amalgamation to render it suitable for the purpose of leather conservation. With a focus on environmental sustainability, we foresee the potential utilization of sky fruit extract in the preservation of leather materials.

Acknowledgement

We convey gratitude to the director of Leather Research Institute and Chairman of Bangladesh Council of Scientific and Industrial Research.

References

1. Kanagaraj, J., John Sundar, V., Muralidharan, C. & Sadulla, S. Alternatives to sodium chloride in prevention of skin protein degradation - A case study. *J. Clean. Prod.* **13**, 825–831, 2005.
2. Technologists, L., Industrial, S. & Officer, D. Raw Hide , Trade and Preservation * Environmental Considerations - Eco-labelling. 1995.
3. Hashem, M. A., Arman, M. N., Sheikh, M. H. R. & Islam, M. M. Sodium chloride substitute for lower salt goat skin preservation: A novel approach. *JALCA* **112**, 270–276, 2017.
4. Uddin, M. M. *et al.* A cleaner goatskin preservation with leaf paste and powder: An approach for salinity remediation in tannery wastewater. *Clean. Eng. Technol.* **6**, 100357, 2022.

5. Wu, J., Zhao, L., Liu, X., Chen, W. & Gu, H. Recent progress in cleaner preservation of hides and skins. *J. Clean. Prod.* **148**, 158–173, 2017.
6. Liknaw, G., Tekalign, T. & Guya, K. Impacts of Tannery Effluent on Environments and Human Health. *J. Environ. Earth Sci.* **7**, 88–97, 2017.
7. Zereen, A., Wahid, A., Khan, Z.-U.-D. & Sardar, A. A. Effect of Tannery Wastewater on the Growth and. *Bangladesh J. Bot.* **42**, 279–285, 2013.
8. Zahid, A. Impact of Tanneries on Groundwater Environment of Dhaka City. (2017).
9. Covington, T. *Tanning Chemistry: The Science of Leather (2nd Edition) — University of Northampton's Research Explorer.* 2019.
10. Abul Hashem, M. *et al.* Phyto-based goatskin preservation to reduce salinity in tannery wastewater. *Clean. Mater.* **4**, 100075, 2022.
11. Vijayalakshmi, K., Judith, R. & Rajakumar, S. Novel plant based formulations for short term preservation of animal skins. *J. Sci. Ind. Res. (India).* **68**, 699–707, 2009.
12. Velappan, B. *et al.* Characterization and application of dried neem leaf powder as a bio-additive for salt less animal skin preservation for tanneries. *Environ. Sci. Pollut. Res.* **29**, 3763–3772, 2022.
13. Nur-A-Tomal, M. S. *et al.* Goatskin preservation with plant oil: significant chloride reduction in tannery wastewater. *Environ. Sci. Pollut. Res.* **28**, 12889–12897, 2021.
14. Sahgal, G. *et al.* Phytochemical and antimicrobial activity of Swietenia mahagoni crude methanolic seed extract. *Trop. Biomed.* **26**, 274–279, 2009.
15. Shivaraj Gouda, T., Kumar, S. C., debnath, S. & Bhattacharjee, C. Antimicrobial Activity of Swietenia mahagoni L (Leaf) Against Various Human Pathogenic Microbes. *Chiranjib Bhattacharjee al. Indo Am. J. Pharm. Res.* **1**, 257–261, 2011.
16. Rahman, A. K. M. S. *et al.* Antibacterial activity of two limonoids from Swietenia mahagoni against multiple-drug-resistant (MDR) bacterial strains. *J. Nat. Med.* **63**, 41–45 , 2009.
17. Hashem, M., Payel, S., Ali, M., Bhowmik, P. & Sahen, M. Tannin agents from native Swietenia microphylla (sky fruit) for leather processing. *Bangladesh J. Sci. Ind. Res.* **58**, 1–8, 2023.
18. Razzaq, M. A., Chowdhury, M. J. & Uddin, M. T. Salt Free Preservation of Raw Goat Skin Using Swietenia Mahogany (Seed) Extract. *JALCA* **117**, 47–53 , 2022.
19. Paritala, V., Chiruvella, K. K., Thammineni, C., Ghanta, R. G. & Mohammed, A. Phytochemicals and antimicrobial potentials of mahogany family. *Revista Brasileira de Farmacognosia* vol. 25 61–83 at https://doi.org/10.1016/j.bjp.2014.11.009, 2015.
20. Suliman, B. Fatty acid composition and antibacterial activity of Swietenia Macrophylla king seed oil. *African J. Plant Sci.* **7**, 300–303, 2013.
21. Sundar, S. Antifungal activity of Swietenia mahogany on Candida albicans and Cryptococcus neoformans. *J. Microbiol. Antimicrob.* **5**, 55–59, 2013.
22. Akter, T., Sarker, S. S., Sujan, S. & Parveen, S. Textile & Leather Review Antimicrobial Activity of Natural and Synthetic Dyes Used in Leather Dyeing: A Comparative Study. doi:10.31881/TLR.
23. Mamun, M. A. Al, Hasan, R., Ahmed, M. R., Paul, A. & Raha, R. Antifungal efficacy of neem leaves (Azadirachta indica) and mahagony fruit bark (Swietenia mahagoni) extracts on leather shoes. *Bangladesh J. Sci. Ind. Res.* **54**, 257–262, 2019.
24. Mecozzi, M., Pietroletti, M., Scarpiniti, M., Acquistucci, R. & Conti, M. E. Monitoring of marine mucilage formation in Italian seas investigated by infrared spectroscopy and independent component analysis. *Environ. Monit. Assess.* **184**, 6025–6036, 2012.
25. Pandey, K. K. & Pitman, A. J. FTIR studies of the changes in wood chemistry following decay by brown-rot and white-rot fungi. *Int. Biodeterior. Biodegrad.* **52**, 151–160, 2003.
26. Dassanayake, R. S., Gunathilake, C., Abidi, N. & Jaroniec, M. Activated carbon derived from chitin aerogels: preparation and CO2 adsorption. *Cellulose* **25**, 1911–1920, 2018.
27. Materials, T. *Bureau of Indian Standard*.,1970.
28. Gunasekera, T. S., Attfield, P. V. & Veal, D. A. A flow cytometry method for rapid detection and enumeration of total bacteria in milk. *Appl. Environ. Microbiol.* **66**, 1228–1232, 2000.
29. American Public Health Association(APHA), American Water Works Association(AWWA) & Water Environment Federation(WEF). Standard Methods for the Examination of Water and Wastewater (21st Edition). *Water Environ. Fed.* 541, 2005.
30. Zapata, F. *et al.* Introducing ATR-FTIR Spectroscopy through Analysis of Acetaminophen Drugs: Practical Lessons for Interdisciplinary and Progressive Learning for Undergraduate Students. *J. Chem. Educ.* **98**, 2675–2686, 2021.
31. Mohammed, S. A., Madhan, B., Demissie, B. A., Velappan, B. & Tamil Selvi, A. Rumex abyssinicus (mekmeko) Ethiopian plant material for preservation of goat skins: Approach for cleaner leather manufacture. *J. Clean. Prod.* **133**, 1043–1052, 2016.
32. Kelly, S. J. R. *et al.* Effect of collagen packing and moisture content on leather stiffness. *J. Mech. Behav. Biomed. Mater.* **90**, 1–10, 2019.
33. Mohammed, S. A., Panda, R. C., Madhan, B. & Demessie, B. A. Rumex abyssinicus (mekmeko) extract as cleaner approach for dyeing in product manufacture: Optimization and modeling studies. *Asia-Pacific J. Chem. Eng.* **13**, 1–19, 2018.
34. Iyappan, K., Ponrasu, T., Sangeethapriya, V., Gayathri, V. S. & Suguna, L. An eco-friendly method for short term preservation of skins/hides using Semecarpus anacardium nut extract. *Environ. Sci. Pollut. Res.* **20**, 6324–6330, 2013.
35. Kanagaraj, J. *et al.* Cleaner techniques for the preservation of raw goat skins. *J. Clean. Prod.* **9**, 261–268 ,2001.
36. Zhang, X., Xu, S., Shen, L. & Li, G. Factors affecting thermal stability of collagen from the aspects of extraction, processing and modification. *J. Leather Sci. Eng.* **2**, 2020.
37. Müller, M. *et al.* Identification of ancient textile fibres from Khirbet Qumran caves using synchrotron radiation microbeam diffraction. *Spectrochim. Acta - Part B At. Spectrosc.* **59**, 1669–1674, 2004.

Lightweight Detection Model for Animal Wet-Blue Hide Surface Defects Based on Yolov5s

by
Qixin Han,[1] Yushan Wan,[1] Luwen Cao,[1] Rong Luo,[2]* Yafei Sun[2] and Weikuan Jia[1]*
[1]*School of Information Science and Engineering, Shandong Normal University*, Jinan 250358, China
[2]*State Key Laboratory of Biobased Materials and Green Papermaking, Qilu University of Technology (Shandong Academy of Science),* Jinan 25035, China

Abstract

In the process of animal leather processing, the surface damage of wet-blue hides restricts the quality of leather products. To ensure the efficiency and quality of animal leather processing, a lightweight model for detecting surface defects on wet-blue hides based on optimized YOLOv5s is proposed. The new model adopts the lightweight EfficientNetV2 network to extract surface defect features and incorporates a spatial pyramid pooling–fast (SPPF) structure at the end of the network to obtain features at different scales. Efficient multi-scale attention (EMA) was embedded in the bottom-up structure of the Neck section to achieve comprehensive feature extraction and retention, ensuring that spatial semantic features are adequately distributed in each feature. A dataset of wet-blue hide defects was constructed and used to verify the performance of the new model. the experimental results show that, the new model is superior to the commonly used classical detection models. The precision rates for detecting three types of leather surface defects, namely imprint, puncture, and breakage, are 86.5%, 95.3%, and 87.9%, respectively. These results can provide technical support for research of surface damage detection in other leather processing applications.

1 Introduction

Leather and its products are among the most traded products in the world, with an annual international trade volume of more than $80 billion.[1] These products encompass a variety of items such as clothing, footwear, and decorative accessories.[2] People's demand for leather is not only practical but also related to the pursuit of aesthetics, thus posing a more stringent challenge to the production of leather products.[3-5] However, surface defects not only cause damage to the appearance of leather but also may have an impact on quality management.[6,7] Therefore, research on the detection of leather surface defects during animal leather processing can help to improve the safety, efficiency and quality of leather production. In the process of animal leather manufacturing, the grading of leather quality currently relies predominantly on manual inspection of the surface defects of wet-blue hides.[8-10] However, this approach faces challenges such as time-consuming processing and significant errors. There is an urgent need for efficient and precise research on the detection of surface defects in wet-blue hides.

Traditional machine learning based methods play an important role in the detection of leather surface defects. Georgieva et al.[11] used rotational invariance and scale invariance of grayscale histograms of leather images for feature analysis processing. On the other hand, Kwak et al.[12] used texture features to identify defects on leather, surfaces and were able to accurately detect a variety of defects, such as pinholes, scratches, and wrinkles, while missing few small defects. Jawahar et al.[13] used an innovative multilevel holding algorithm to segment the leather surface defect region to objectively quantify the leather surface defects and demonstrated the potential of classifying leather defects. Gan et al.[14] proposed an automatic leather defect localization and detection system using AlexNet as a feature descriptor and support vector machine (SVM) as a classifier to determine the presence or absence of defects on leather patches. Jawahar et al.[15] proposed an SVM classifier image processing technique based on wavelet features that can automatically identify leather blemish defects. Although the above methods have achieved a series of results in the process of defect detection, some of the defect features are difficult to extract due to the influence of noisy environmental factors in the processing workshop, which further restricts the detection accuracy of surface defects.

Deep learning methods, which can learn features directly from raw data, have been widely used in the fields of surface defect detection,[16,17] equipment fault diagnosis[18] and medical imaging[19] and have achieved remarkable results; inspired by these methods, deep learning theory has been introduced into the detection of surface defects in animal leather. For example, Liong et al.[20] developed an automatic defect detection technique based on AlexNet and U-Net to classify leather images into three categories (normal, black lines, and wrinkles) to achieve accurate pixel-level defect location. Liong et al.[21] reduced the number of defect boundary points while maintaining the shape of the defects for tick bite damage, and ultimately used a robotic arm to automatically outline the boundaries of the defects on the leather surface. Luo et al.[22] proposed a robust breakage detection network (RBD-Net) model for leather breakage detection, which can effectively address various interfering factors and ensure reliable detection of leather in

*Corresponding authors email: R Luo, lrcity@qlu.edu.cn ; WK Jia, jwk_1982@163.com
Manuscript received January 30, 2024, February 26, 2024.

practical applications. Iqbal et al.[23] developed an automated system for detecting defects in leather images based on visual surface analysis and introduced a multi-layer residual convolutional neural network (MLR-Net), which effectively and accurately identifies and segments defects in leather images. In comparison to traditional machine learning algorithms, the aforementioned defect detection algorithm exhibits significantly improved accuracy and robustness.

Current algorithms are mostly designed to operate under ideal conditions. Faced with noisy processing environments, factors such as lighting, defect types, and shapes can significantly impact the efficient and accurate detection of surface defects on wet-blue hides. In the large-scale production process of animal leather, achieving real-time and efficient detection is crucial. Employing lightweight detection models can meet this requirement while providing effective solutions and reducing hardware costs. Furthermore, with the proliferation of industrial smart devices such as robots and intelligent cameras, deploying lightweight detection models on these embedded devices is more feasible, thereby enhancing system flexibility and scalability. The mentioned lightweight model is characterized by reduced parameter count and computational complexity, while also demonstrating faster detection and inference speeds. Therefore, this study proposed a lightweight detection model based on optimized YOLOv5s. The primary contributions of this study include the following:

(1) The introduction of the lightweight EfficientNetV2 network is employed to extract surface defect features from wet-blue hides, thereby reducing the model's parameter count. This approach aims to address the challenges associated with inadequate feature extraction and low training efficiency.

(2) Introducing the spatial pyramid pooling–fast (SPPF) structure at the end of the backbone network facilitates the fusion of features across multiple scales. Additionally, embedding efficient multi-Scale attention (EMA) in the bottom-up structure of the Neck section ensures the effective distribution of spatial semantic features, achieving cross-space multi-scale aggregation.

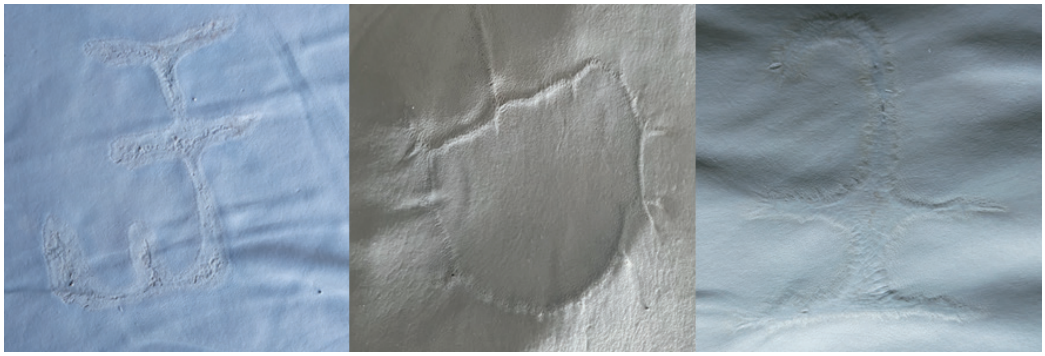

a) Brand

b) Broken hole

c) Broken surface

Figure 1. Three Different Types of Defects

(3) Considering issues such as overlapping areas and geometric features of detection boxes, the complete IoU (CIoU) loss is employed as the regression loss function, to enhance the convergence speed and performance of the network.

The rest of the paper is organized as follows. Section 2 introduces the dataset. Section 3 describes the proposed method. Section 4 conducts experiments and analyzes the results. Finally, Section 5 summarizes the work.

2 The wet-blue hide defect dataset

2.1 Image acquisition

The leather images selected for this study were obtained from preliminarily processed cowhides, resulting in wet-blue hides. The details of the acquisition are outlined below:

Defect types: Images were collected for three distinct surface defect types on wet-blue hides: punctures, breaks, and imprints. Figure 1 provides examples of wet-blue hide images depicting these three types of defects.

Collection sites: The data collection was conducted at Shandong Dexin Leather Co., Ltd. and Zibo Dahuan Jiubao'en Leather Group Co., Ltd., both of which are located in Zibo city, Shandong Province, China.

Collection environment: The processing environment of wet-blue hides is inherently complex. To simulate the actual factory conditions as closely as possible, a diverse set of leather images was collected. These images encompassed various time periods, different shooting angles and distances, diverse lighting conditions, and different types of interference and damage. Samples closer to the camera were treated as large targets, while those farther away served as small targets, thereby enriching the dataset comprehensively.

Equipment for data acquisition: The wet-blue hide images were captured using both smartphones and a Sony Alpha 7 II camera, resulting in a total of 2162 images. To enhance the network's detection quality for low-resolution images under real-time detection requirements, the images were compressed and uniformly scaled to 800 pixels × 600 pixels.

2.2 Data augmentation

Training a detection model often relies on a sufficient amount of sample data. Therefore, to enhance the model's generalizability and stability, and to further improve its detection accuracy while avoiding overfitting due to insufficient data collection, this study employs Mosaic data augmentation[24] to process the input images. In each iteration cycle (Epoch), this method randomly replaces images. The replacement involves random scaling, random cropping, and random arrangement to generate new images. During the training process, images with different combinations are reconfigured in the subsequent iteration cycle, thereby enhancing the network's generalization capability. Figure 2 shows the annotated images after surgery with Mosaic data augmentation.

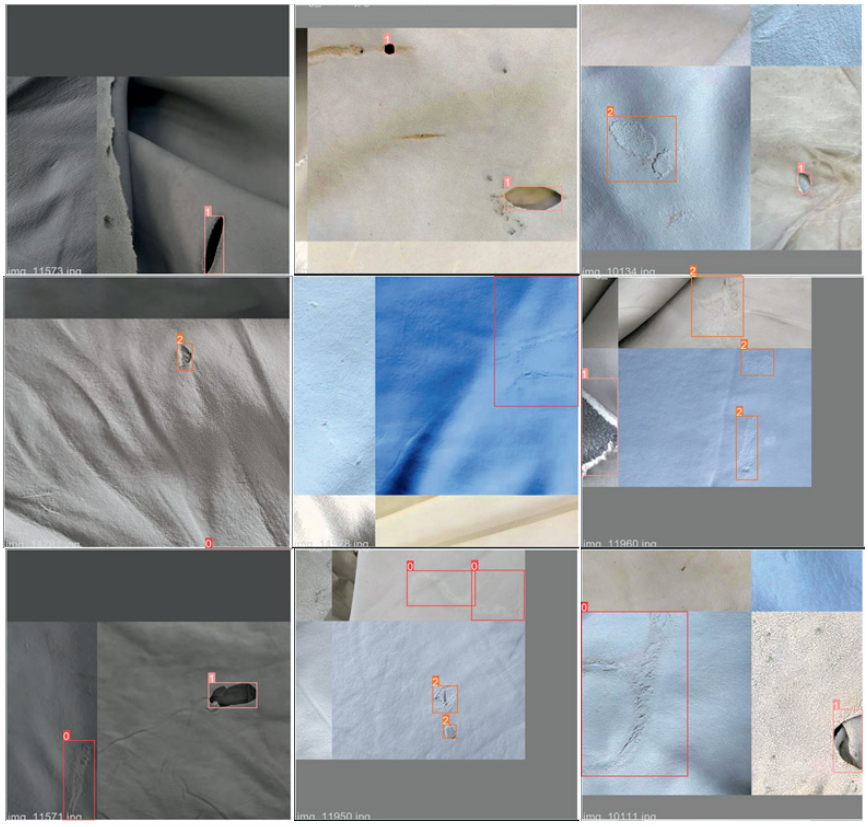

Figure 2. Mosaic Data Augmentation

Table I

Statistical Summary of Defect Quantities by Different Sizes.

	small target	medium target	large target	total
Training Set	260	236	1776	2272
Validation Set	150	129	750	1029
Total	410 (12.42%)	365 (11.06%)	2526 (76.52%)	3301

2.3 Dataset creation

First, the leather defect dataset images were effectively annotated using LabelMe software, with labels categorized as Brand, Broken hole, and Broken surface. The annotated points denote the damaged regions on the wet-blue hides, while the remaining areas serve as the background. All the annotation information is stored in JSON files corresponding to the original images, and these JSON files are converted into a leather defect dataset in Microsoft COCO format.[25] Following the annotation of target areas, defects are further categorized into small, medium, and large sizes based on the following criteria:

$$\text{small target: area} \le 32^2.$$
$$\text{medium target: } 32^2 < \text{area} \le 96^2.$$
$$\text{large target: area} > 96^2$$

Finally, based on the generated dataset, the data were partitioned into training and validation sets at a 7:3 ratio. The annotation information for each dataset was consolidated, forming the ultimate wet-blue hide surface defect dataset. The quantity of defects of different sizes in the dataset is presented in Table I.

3 Lightweight detection model for surface defects on wet-blue hides

Object detection networks are generally complex and involve large model sizes. To improve the efficiency and quality of animal leather processing, this study proposes a lightweight detection model tailored for surface defects on wet-blue hides based on the YOLOv5s model. This model not only allows for rapid and efficient identification of surface defects but also facilitates deployment on embedded devices. As illustrated in Figure 3, the overall network is primarily divided into four parts: Input, Backbone, Neck, and Output. The Backbone stage utilizes the EfficientNetV2[26] +SPPF structure to reduce model complexity and expedite training. The Neck stage adopts the feature pyramid network (FPN)+bottom-up[27] structure and embeds the EMA attention module[28] into the bottom-up structure, enabling better retention of spatial semantic features and improved fusion of multiscale features. The output layer of the network employs the CIoU loss[29] as the loss function.

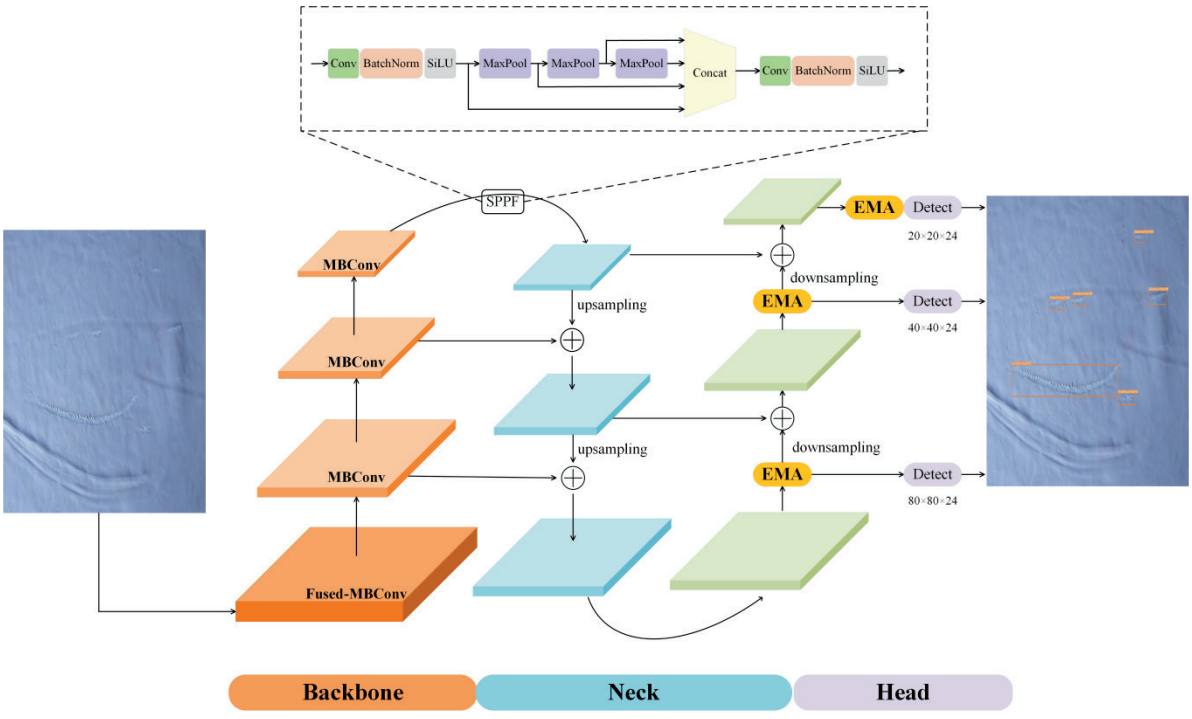

Figure 3. Lightweight Detection Model for Surface Defects on Wet-Blue Hides

3.1 Defect feature extraction architecture

In the intricate production processes of animal leather processing, ensuring that the detection equipment can accurately discern surface defects on leather is of paramount importance. To achieve this goal, embedding a fast and straightforward network model into the detection equipment becomes imperative. This allows for efficient detection of surface defects on animal leather in complex environments while ensuring precise classification and processing of the animal leather. In this study, the backbone network of the new model utilizes the compact yet powerful EfficientNetV2 network and the SPPF structure.

The EfficientNetV2 model[30] is characterized by its compact size, fast training speed, and high parameter efficiency, and is achieved through the utilization of multiple convolutions with a stride of 2 to reduce the data size. The network architecture of EfficientNetV2 is presented in Table II. This architecture employs fewer parameters to attain higher accuracy and efficiency, thereby striking a balance between model precision and operational speed.

The EfficientNetV2 network is primarily composed of shallow Fused-MBConv and deep MBConv layers, as illustrated in Figure 4.

Table II

The architecture of the EfficientNetV2 network

Stage	Operation	Stride	Channels	Layers
0	Conv3×3	2	24	1
1	Fused-MBConv1 k3×3	1	24	2
2	Fused-MBConv4 k3×3	2	48	4
3	Fused-MBConv4 k3×3	2	64	4
4	MBConv4, SE0.25 k3×3	2	128	6
5	MBConv6 ,SE0.25 k3×3	1	160	9
6	MBConv6,SE0.25 k3×3	2	256	15
7	Conv1×1 & Pooling & FC	-	1280	1

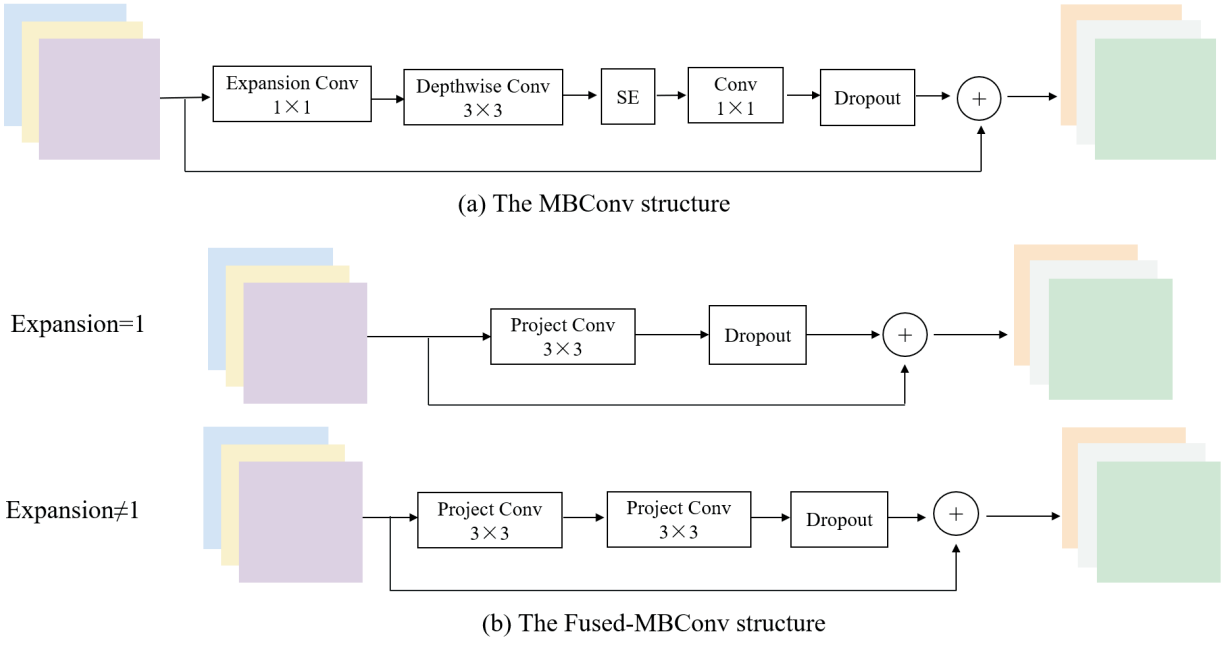

Figure 4. The Fused-MBConv and MBConv structures

In the MBConv module, depth wise separable convolution is employed, where each convolution kernel is responsible for one input channel, meaning that each channel is convolved by only one kernel. The number of channels obtained on the feature map is exactly consistent with the number of input channels. This convolution comprises depth wise convolution and pointwise convolution. The Fused-MBConv module replaces Depth wise Conv3×3 and Expansion Conv1×1 in MBConv with the standard Conv3×3. Through the combination of training-aware Neural Architecture Search (NAS) and scaling, both modules work collaboratively to optimize the model's training speed and parameter efficiency.

While the rational combination of the aforementioned two modules significantly reduces the number of parameters and computations, there is a trade-off in terms of feature extraction efficacy. This is because the modified feature extraction network, as part of the streamlined model, loses a portion of the feature information. To mitigate the risk of excessive information loss, an SPPF structure is added after the EfficientNetV2 network architecture. This structure utilizes pooling kernels of different sizes to extract features at various scales, capture objects at different scales, and better understand the contextual information in the input image. This addition aims to alleviate the problem of information loss.

3.2 EMA attention module

To better integrate the defect features extracted by the backbone network, EMA attention is embedded in the bottom-up structure of the Neck section. This approach facilitates the spatial aggregation of multiscale features, ensuring an improved distribution of spatial semantic features within each feature. The structure of EMA attention comprises three main components: Feature Grouping, Parallel Subnetworks, and Cross-spatial learning, as illustrated in Figure 5.

First, the EMA divides any given feature map into G sub-features along the channel dimension to learn different semantics. Second, within the parallel subnets, the EMA employs three parallel routes to extract attention weight descriptors for grouped feature maps. Two parallel routes employ two one-dimensional global average pooling operations encoding channels along two spatial directions, and the third route merely stacks a single 3×3 kernel to capture multiscale feature representations. Finally, in cross-space learning, two tensors are introduced to encode the global spatial information via two-dimensional global average pooling for the outputs of the two branches in the parallel subnet. The corresponding outputs are subsequently transformed into the respective dimensional shapes, denoted as $R_1^{1\times C//G} \times R_3^{C//G\times H*W}$ and $R_3^{1\times C//G} \times R_1^{C//G\times H*W}$, before being subjected to the joint activation mechanism of channel features. The employed two-dimensional global average pooling is expressed as follows:

$$Z_c = \frac{1}{H\times W}\sum_j^H \sum_i^W x_c(i,j) \tag{1}$$

which is designed to encode global information and model long-range dependencies, where, x_c represents the input feature at the *c-th* channel, C represents the number of input channels, and H and W represent the spatial dimensions of the input feature.

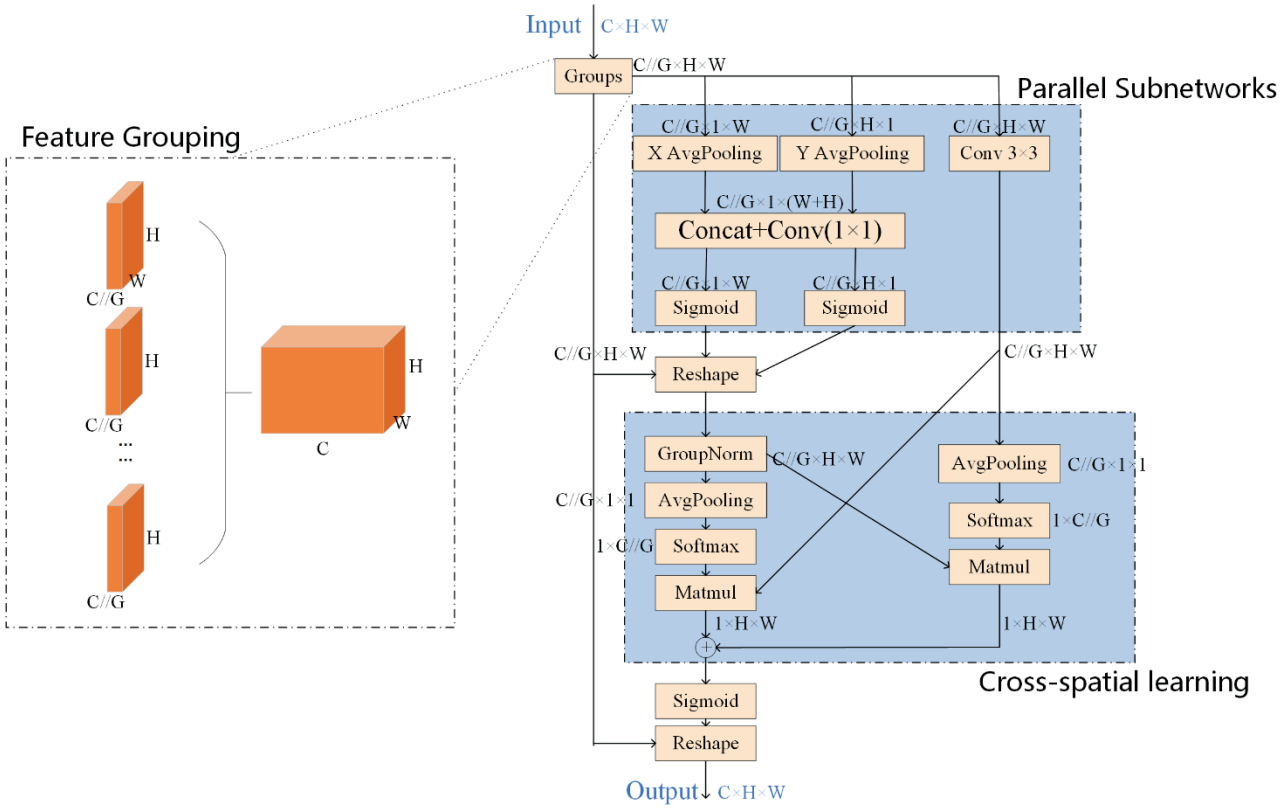

Figure 5. Diagram of the Efficient Multi-Scale Attention Structure

Introducing EMA attention allows focused retention of information in each channel while reducing computational overhead. It redefines a portion of channels on a batch level and divides the channel dimension into multiple sub-features, ensuring that spatial semantic features are well-distributed within each feature. This approach addresses issues such as unclear edges in defect images, where regions formed by the leather edge and the input image boundary are prone to being mistakenly identified as punctures. Consequently, this approach enhances the ability of the model to detect surface defects on leather surfaces.

3.3 The CIoU loss function

The choice of a loss function plays a crucial role in model training and is vital for optimizing the iterative process and achieving optimal training results through gradient backpropagation. This study enhances the loss function of the YOLOv5s model to improve its ability to detect surface defects on leather surfaces. The loss function for YOLOv5s is presented in Formula (2), which consists of three parts, with λ_1, λ_2, λ_3, as the balance coefficient. The first part, loss_cls, employs the binary cross entropy (BCE) loss to calculate the classification loss, focusing solely on positive samples. In the second part, loss_loc, the generalized IoU (GIoU) loss is utilized to compute the regression loss for only positive samples. Finally, loss_conf employs the BCE loss to calculate the target confidence loss for all samples.

$$\text{Loss} = \lambda_1 L_{\text{cls}} + \lambda_2 L_{\text{loc}} + \lambda_3 L_{\text{conf}} \tag{2}$$

However, when two prediction boxes overlap completely, the GIoU metric fails to accurately reflect the distance and positional relationship between the prediction box and the ground truth box. When the GIoU values are equal, the overlap effect of the two boxes may differ, making it challenging to quickly and accurately determine the optimization direction for the localization box. The CIoU loss function addresses this limitation by incorporating the Euclidean distance between the prediction box and the ground truth box, as well as the loss of the detection box scale, into the penalty term. This approach enhances the aspect ratio of the target box, progressively bringing the prediction box closer to the ground truth box during continuous training, thereby improving the convergence speed and regression accuracy of the network. Consequently, the model proposed in this study replaces the regression loss function with the CIoU loss, and the penalty term of the CIoU loss is shown in Formula (3).

$$\mathfrak{R}_{CIoU} = \frac{\rho^2(b,b^{gt})}{c^2} + \alpha v \tag{3}$$

$$\alpha = \frac{v}{(1\text{-}IoU)+v} \tag{4}$$

$$v = \frac{4}{\pi^2}\left(arctan\ \frac{w^{gt}}{h^{gt}} - arctan\ \frac{w}{h}\right)^2 \tag{5}$$

Where α is a positive balancing parameter, v measures the consistency of aspect ratios, b and b^{gt} represent the center coordinates of the predicted and ground truth boxes, respectively; $\rho(b, b^{gt})$ is the Euclidean distance between the center coordinates of the predicted and ground truth boxes; c is the Euclidean distance between the two diagonal vertices of the minimum bounding rectangle for the predicted and ground truth boxes; w, h, w^{gt} and h^{gt} are the widths and heights of the predicted and ground truth boxes, respectively; and intersection over union (IoU) is the intersection over union between the predicted and ground truth boxes. Thus, the CIoU loss is defined as follows:

$$L_{CIoU} = 1 - IoU + \frac{\rho^2(b,b^{gt})}{c^2} + \alpha v \tag{6}$$

The introduction of the CIoU loss expedites model convergence, addressing the drawback where gradients were ineffective at backpropagation when the predicted box overlaps with the ground truth box. This enhancement results in more stable regression for the target box.

4. Experiments

To better validate the effectiveness of the model in detecting surface defects on animal leather, this study conducted the following experiments, providing detailed descriptions of the experimental setup and performing comparative analyses of the results. First, a detailed description of the experimental platform was provided. Second, experimental details for both the training and testing phases were outlined. For the training process, the optimal model was selected and applied to the validation set, allowing for a comparison and evaluation of the experimental results. Finally, comparative experiments were conducted using existing classical object detection algorithms under the same experimental configuration to assess the performance of the proposed model in this study.

4.1 Experimental operating platform

All the experiments conducted in this study were completed on the same server system, which is primarily configured with the Ubuntu 16.04 LTS operating system. The processor utilized is an Intel® Xeon(R) Silver 4214R CPU @ 2.40 GHz × 45, complemented by a 10 GB NVIDIA GeForce RTX 3080 GPU and V11.4 CUDA environment. All the models are executed using the Python language and the PyTorch 1.7 deep learning library.

4.2 Details of the experimental implementation

To conduct more effective experiments, enhance the model's adaptability to the dataset, and improve the detection accuracy of surface defects on leather, the image size is standardized to (800, 600) before feeding it into the training network. During formal training, a small-batch method is employed for 300 epochs of iteration. After each epoch, the model's training status is validated using the validation set. This approach facilitates better adjustment of hyperparameters to obtain optimal values and enhances the overall efficiency of the model.

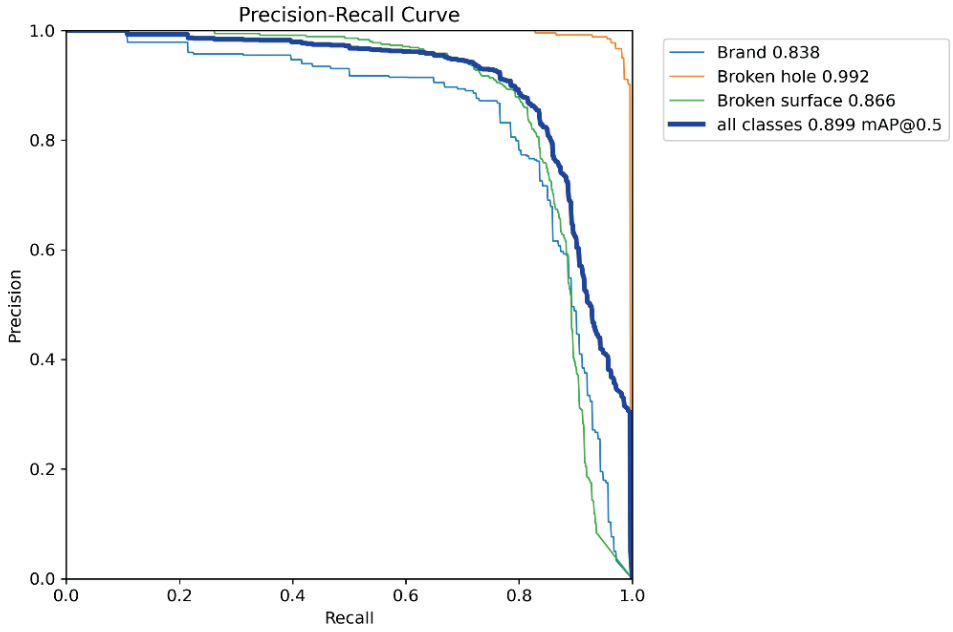

Figure 6. The Precision-Recall (PR) curve for model training

Weights are normalized using batch normalization at each refreshment, and model parameters are updated using stochastic gradient descent. During the training process, the learning rate, weight decay, and momentum are set to 0.01, 0.0005, and 0.900, respectively. The training progress of the model is illustrated in Figure 6.

4.3 Evaluation criteria

As the model needs to accurately predict the results of surface defect detection on leather, this experiment employs precision and recall as evaluation metrics for the model's effectiveness. The precision is calculated using Formula (7), and the recall is calculated using Formula (8).

$$precision = \frac{TP}{TP + FP} \tag{7}$$

$$recall = \frac{TP}{TP + FN} \tag{8}$$

Where *TP, FP, FN* and *TN* represent the sample quantities of true positive, false positive, false negative, and true negative instances of defects, respectively. To comprehensively evaluate the model, further calculations are performed using Formula (9) to compute the Average Precision (AP) metric at specified *IoU* thresholds and *mAP*, as per Formula (10), to assess the mean average precision.

$$AP = 1/101 \sum_{r \in R} P(r) \tag{9}$$

$$mAP = 1/n \sum_{i=\mathrm{I}}^{n} AP_i \tag{10}$$

Where the letter *r* represents the recall, and *R* is the set of recall rates, which consists of 101 values: [0.0, 0.01, 0.02, ..., 0.98, 0.99, 1.0]. P(r) denotes the precision related to the recall rate. The letter *i* represents the *IoU* threshold, and *I* is the set of *IoU* thresholds, comprising 10 values: [0.5, 0.55, 0.6, 0.65, ..., 0.9, 0.95]. n is the number of categories, and in this study, n is set to 3, corresponding to three defect categories.

When the predicted category of a defect on the leather surface is correct and the *IoU* is greater than a certain threshold (the *IoU* threshold in the experiment is set to 0.5), the detection result is considered correct. The model's evaluation results for the detection of three different defect types in the leather dataset are presented in Table III, and the actual detection performance of the three defects is shown in Figure 7.

Table III

Results of Comparative Evaluations for Defect Detection in Three Leather Categories

Type	Precision/%	Recall/%	mAP@.5/%	mAP@.5:.95/%
Brand	86.5	76.6	83.8	52.5
Broken hole	95.3	98.1	99.2	80.9
Broken surface	87.9	79.9	86.6	55.8

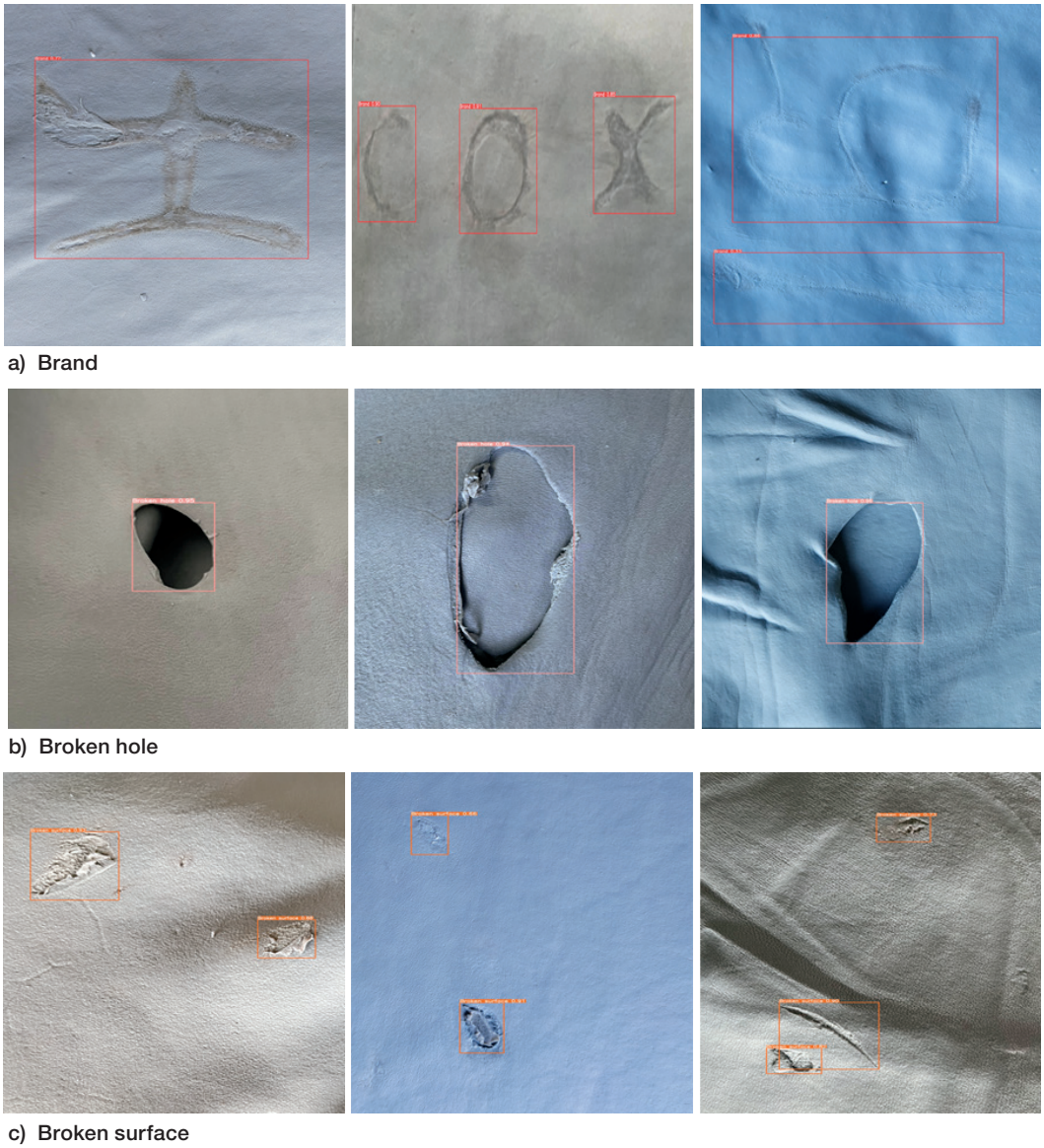

Figure 7. Results of Leather Surface Defect Detection

4.4 Ablation studies

In this section, the effectiveness of the model's backbone network and attention module was validated through ablation studies. To comprehend the contributions of the EfficientNetV2 network, EMA attention module, and CIoU loss function to detection efficiency and accuracy, the original backbone network is used as a baseline for comparison against the impacts of EfficientNetV2, EMA, and CIoU loss.

Table IV

The Impact of the EfficientNetV2 and EMA Modules on the Experimental Results

Baseline Model	Backbone Network	EMA Attention	Loss Function	precision/%	recall/%	mAP@.5/%	Params/M
YOLOv5s	CSPDarknet	×	GIoU loss	87.5	84.8	88.3	7.03
	EfficientNetV2	√	GIoU loss	88.7	84.8	89.2	5.60
	EfficientNetV2	×	CIoU loss	91.5	82.8	89.0	5.60
	CSPDarknet	√	CIoU loss	87.4	86.3	88.4	7.03
YOLO v5s	EfficientNetV2	√	CIoU loss	89.6	84.9	89.9	5.60

As shown in Table IV, when the backbone network is replaced with EfficientNetV2 and the CIoU loss is utilized as the loss function, the improvement in accuracy is most pronounced, with an increase of 4%. When using the original backbone network and incorporating EMA attention with CIoU loss as the loss function, the *recall* rate shows the most significant improvement, increasing by 1.5%. Furthermore, when all three factors work together, all three metrics improve, with the *mAP* experiencing the most notable increase, increasing by 1.6%. When EfficientNetV2 is employed as the backbone network for all the cases, the model's parameter count decreases by 1.43M. These results indicate that the improved YOLOv5s model not only effectively reduces the model's parameter count but also enhances the detection accuracy, validating the effectiveness of the various modules in the new model.

4.5 Comparison experiments

To validate the detection performance of the improved YOLOv5s model, comparisons were made with classical and state-of-the-art detection algorithms, including Faster R-CNN,[31] FSAF,[32] Mask R-CNN,[33] Grid RCNN,[34] Yolact,[35] YOLOv3,[36] and YOLOv5s. The experiments were conducted in the same environment using identical equipment and image preprocessing procedures. Following model detection, a uniform application of Non-Maximum Suppression (NMS) and the same *IoU* threshold was employed for filtering. The specific experimental results are presented in the following table. Notably, the value of the *mAP* is particularly emphasized because it accurately reflects the detection accuracy of leather defect types, facilitating subsequent determination of leather grades and corresponding processing. Thus, the *IoU* threshold of 0.5 and the *mAP* corresponding to small, medium, and large targets were selected as the comparative evaluation metrics.

According to the results presented in Table V, the improved model achieved a *mAP* of 89.9%. For large targets with an *IoU* threshold of 0.5, the AP values were 67.1% and 74.4%, generating an $AR_{maxDet=100}$ of 76.2%. According to the results presented in Table VI, the model's parameter count is 5.60M, surpassing the metrics of other comparative models. However, to ensure the precision of detection, the model's frames per second (FPS) and inference time do not reach the optimal level. Therefore, the improved model exhibits superior detection capabilities and lower computational complexity. Moreover, in comparison with the actual detection results of YOLOv5s shown in Figure 8, the improved YOLOv5s demonstrate finer handling of regions formed by the leather edge and image boundary, avoiding misidentifying edge regions as puncture damage.

Table V

The detection results of both classical and state-of-the-art detection models for leather defects.

Model	Backbone Network	mAP/%	AP_s/%	AP_m/%	AP_l/%	$AR_{maxDet=100}$/%
Faster RCNN	ResNet50	83.9	32.3	60.3	63.7	70.0
Mask RCNN	ResNet50	71.7	26.6	45.6	50.7	57.4
Grid RCNN	ResNet50	84.6	40.9	63.1	67.6	74.5
FSAF	ResNet50	81.5	52.7	55.1	57.1	67.7
Retinanet	ResNet50	82.7	54.2	60.3	65.1	71.4
Yolact	ResNet50	73.0	18.9	44.8	52.6	55.1
YOLO v3	Darknet-53	85.8	35.3	63.4	65.6	69.4
YOLO v5s	CSPDarknet	88.3	41.0	63.9	73.6	75.5
Ours	EfficientNetV2	89.9	38.9	67.1	74.4	76.2

Table VI

The parameter count, computational complexity, and detection performance outcomes of the detection model.

Model	Backbone Network	Params/M	FPS/s	Inference time/ms	Flops/GFLOPs
Faster RCNN	ResNet50	41.3	16.0	62.1	71.7
Mask RCNN	ResNet50	44.4	12.7	78.7	125.0
Grid RCNN	ResNet50	64.5	9.8	102.0	291.0
FSAF	ResNet50	36.4	12.9	77.5	60.7
Retinanet	ResNet50	38.0	14.1	70.9	61.5
Yolact	ResNet50	34.8	36.2	27.6	61.3
YOLO v3	Darknet-53	62.0	18.3	54.6	58.6
YOLO v5s	CSPDarknet	7.0	45.2	20.9	16.0
Ours	EfficientNetV2	5.6	25.9	37.5	6.9

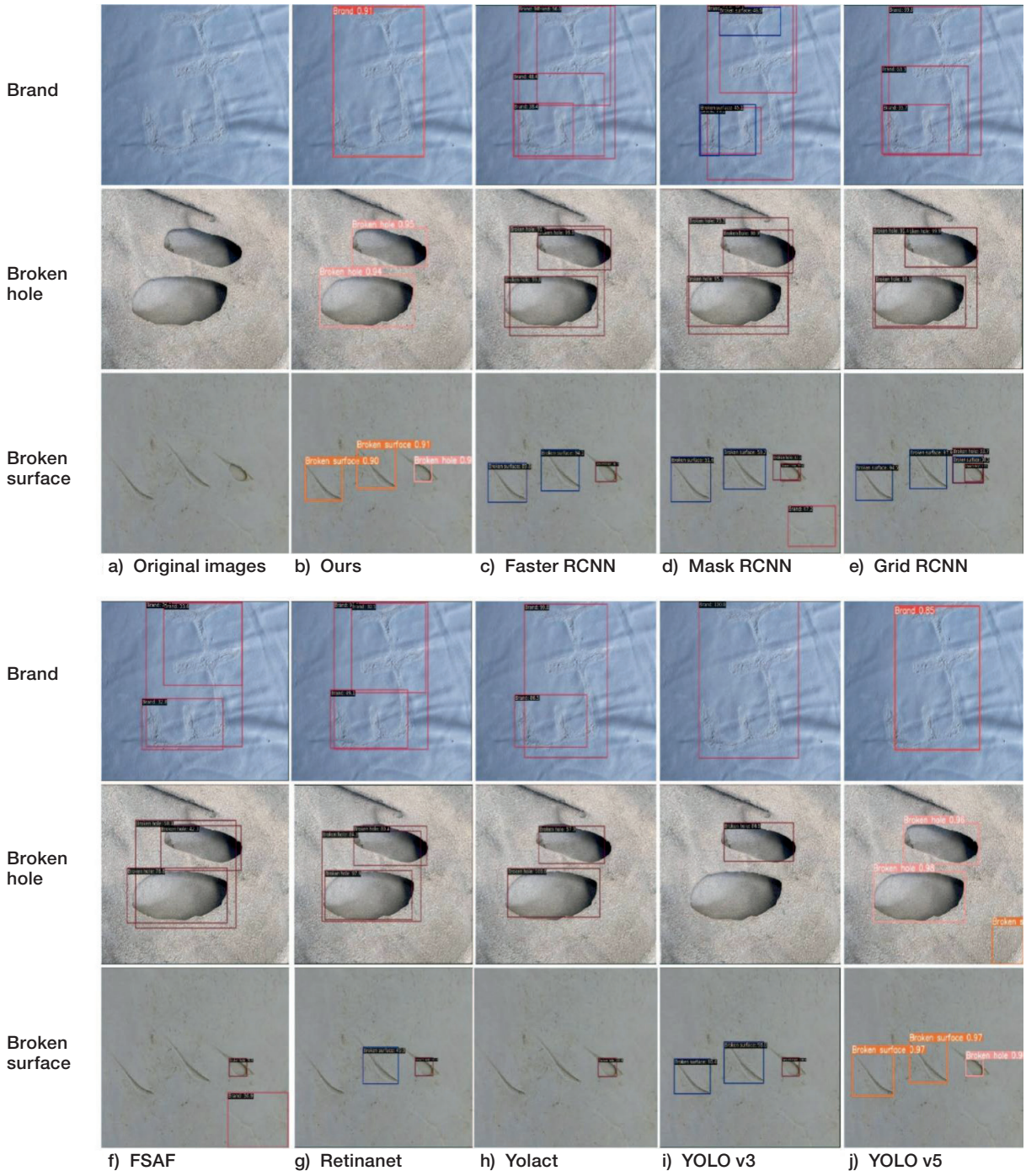

Figure 9. Comparison of Detection Images in the Wet-Blue Hide Dataset

The above analysis indicates that the improved detection model, which has the characteristics of a simple network structure, low computational complexity, and fast model speed, achieves high detection accuracy. This ensures a balance between accuracy and speed, making it suitable for application in animal leather production inspection. The improved model can be deployed in the leather surface defect detection process on production lines. Figure 9 shows a comparison of the images detected in the wet-blue hide dataset.

5. Conclusion

Addressing the issue of surface defect detection in animal leather, this research optimizes the YOLOv5s model tailored to different defect types, thereby achieving robust results in leather surface defect detection. In the proposed model, the EfficientNetV2 network and SPPF structure replace the original backbone network, effectively reducing the parameter count and computational complexity while maintaining high accuracy. Additionally, the EMA attention

module is embedded in the Neck section, preserving semantic features extracted from space more effectively and ensuring their distribution across each feature. Finally, in the Head section of the model, a more precise CIoU loss is employed as the regression loss function, which not only accelerates the model convergence but also ensures more stable regression.

This study focused on surface defects in wet-blue hides in animals and presents an improved lightweight detection model based on YOLOv5s. The model exhibits a 23% reduction in parameters, achieving the *mAP* of 89.9%. In comparison to other lightweight networks, the proposed algorithm not only reduces the number of parameters but also maintains high accuracy. This makes it more suitable for deployment on mobile devices with limited computational resources, facilitating efficient detection and identification of surface defects in animal leather.

By simulating scenarios in animal leather production, this model demonstrates the ability to overcome various interferences, enabling cost-effective detection and exhibiting strong stability. Given the model's efficiency in detecting surface defects on animal leather, its detection algorithm can be extended to other production inspection contexts. While the model achieves efficient detection results, the complexity of production work needs to be taken into consideration. Future research may focus on further enhancing the model's efficiency and practical operability.

Acknowledgments

This work is supported by National Nature Science Foundation of China (No.: 21978139); Natural Science Foundation of Shandong Province in China (ZR2019MB030); New Twentieth Items of Universities in Jinan (2021GXRC049).

References

1. Omoloso O, Mortimer K, Wise W R, et al. Sustainability research in the leather industry: A critical review of progress and opportunities for future research. *Journal of Cleaner Production*, 2021, 285: 125441.
2. Cadirci B H, Ozgunay H, Vural C, et al. A new defect on leather: Microbial bio-film. *JALCA* 2010, **105**(04): 129-134.
3. Aslam M, Naqvi S S, Khan T M, et al. Trainable guided attention based robust leather defect detection. *Engineering Applications of Artificial Intelligence*, 2023, **124**: 106438.
4. Jawahar M, Babu N K C, Vani K, et al. Vision based inspection system for leather surface defect detection using fast convergence particle swarm optimization ensemble classifier approach. *Multimedia Tools and Applications*, 2021, **80**: 4203-4235.
5. Mohammed K M C, Kumar S S, Prasad G. Optimized fuzzy c-means clustering methods for defect detection on leather surface. *Journal of Scientific and Industrial Research*, 2020, **79**(9): 833-836.
6. Liu Y, Yuan Y, Liu J. Deep learning model for imbalanced multi-label surface defect classification. *Measurement Science and Technology*, 2021, **33**(3): 035601.
7. Liu X, He W, Zhang Y, et al. Effect of dual-convolutional neural network model fusion for Aluminum profile surface defects classification and recognition. *Mathematical Biosciences and Engineering*, 2022, **19**(1): 997-1025.
8. Aslam M, Khan T M, Naqvi S S, et al. An ensemble of fine-tuned deep learning networks for wet-blue leather segmentation. *JALCA* 2022, **117**(4).
9. Aslam M, Khan T M, Naqvi S S, et al. Ensemble convolutional neural networks with knowledge transfer for leather defect classification in industrial settings. IEEE Access, 2020, 8: 198600-198614.
10. Aslam M, Khan T M, Naqvi S S, et al. Learning to recognize irregular features on leather surfaces. *JALCA* 2021, **116**(5).
11. Georgieva L, Krastev K, Angelov N. Identification of surface leather defects. *CompSysTech*, 2003, **3**, 303–307.
12. Kwak C, Ventura JA, Tofang-Sazi K. Automated defect inspection and classification of leather fabric. *Intelligent Data Analysis*, 2001, **5**(4):355–370.
13. Jawahar, M., & Vani, K. Machine vision inspection system for detection of leather surface defects. *JALCA* 2019, **114**(1), 10–19.
14. Gan Y S, Liong S T, Zheng D, et al. Detection and localization of defects on natural leather surfaces. *Journal of Ambient Intelligence and Humanized Computing*, 2021: 1-15.
15. Jawahar M, Babu N K C, Vani K. Leather texture classification using wavelet feature extraction technique. 2014 IEEE International Conference on Computational Intelligence and Computing Research. IEEE, 2014: 1-4.
16. Saberironaghi A, Ren J, El-Gindy M. Defect detection methods for industrial products using deep learning techniques: A review. *Algorithms*, 2023, **16**(2): 95.
17. Aslam M, Khan T M, Naqvi S S, et al. Putting current state of the art object detectors to the test: towards industry applicable leather surface defect detection. 2021 *Digital Image Computing: Techniques and Applications* (DICTA). IEEE, 2021: 01-08.
18. Kaya Y, Kuncan F, ERTUNÇ H M. A new automatic bearing fault size diagnosis using time-frequency images of CWT and deep transfer learning methods. *Turkish Journal of Electrical Engineering and Computer Sciences*, 2022, **30**(5): 1851-1867.
19. Kaya Y, Yiner Z, Kaya M, et al. A new approach to COVID-19 detection from X-ray images using angle transformation with GoogleNet and LSTM. *Measurement Science and Technology*, 2022, **33**(12): 124011.
20. Liong S T, Zheng D, Huang Y C, et al. Leather defect classification and segmentation using deep learning architecture. *International Journal of Computer Integrated Manufacturing*, 2020, **33**(10-11): 1105-1117.
21. Liong S T, Gan Y S, Huang Y C, Yuan C A, Chang H C. Automatic defect segmentation on leather with deep learning. arXiv preprint arXiv: 1903.12139, 2019.
22. Luo R, Chen R, Jia F, et al. RBD-Net: robust breakage detection algorithm for industrial leather. *Journal of Intelligent Manufacturing*, 2023, **34**(6): 2783-2796.
23. Iqbal S, Khan T M, Naqvi S S, et al. MLR-Net: A multi-layer residual convolutional neural network for leather defect segmentation.

Engineering Applications of Artificial Intelligence, 2023, 126: 107007.
24. Bochkovskiy A, Wang C Y, Liao H Y M. Yolov4: Optimal speed and accuracy of object detection. arXiv preprint arXiv:2004.10934, 2020.
25. Lin T Y, Maire M, Belongie S, et al. Microsoft coco: Common objects in context. Computer Vision–ECCV 2014: 13th European Conference, Zurich, Switzerland, September 6-12, 2014, Proceedings, Part V 13. Springer International Publishing, 2014: 740-755.
26. Tan M, Le Q. Efficientnetv2: Smaller models and faster training. International conference on machine learning. *PMLR*, 2021: 10096-10106.
27. Liu S, Qi L, Qin H, et al. Path aggregation network for instance segmentation. Proceedings of the IEEE conference on computer vision and pattern recognition. 2018: 8759-8768.
28. Ouyang D, He S, Zhang G, et al. Efficient Multi-Scale Attention Module with Cross-Spatial Learning. ICASSP 2023-2023 IEEE International Conference on Acoustics, Speech and Signal Processing (ICASSP). IEEE, 2023: 1-5.
29. Zheng Z, Wang P, Liu W, et al. Distance-IoU loss: Faster and better learning for bounding box regression. Proceedings of the AAAI conference on artificial intelligence. 2020, **34**(07): 12993-13000.
30. Tan M, Le Q. Efficientnet: Rethinking model scaling for convolutional neural networks. International conference on machine learning. *PMLR*, 2019: 6105-6114.
31. Ren S, He K, Girshick R, et al. Faster R-CNN: towards real-time object detection with region proposal networks. International Conference on Neural Information Processing Systems. MIT Press, 2015:91-99.
32. Zhu C, He Y, Savvides M. Feature selective anchor-free module for single-shot object detection. Proceedings of the IEEE/CVF conference on computer vision and pattern recognition. 2019: 840-849.
33. He K, Gkioxari G, Dollár P, et al. Mask r-cnn. Proceedings of the IEEE international conference on computer vision. 2017: 2961-2969.
34. Lu X, Li B, Yue Y, et al. Grid r-cnn. Proceedings of the IEEE/CVF Conference on Computer Vision and Pattern Recognition. 2019: 7363-7372.
35. Bolya D, Zhou C, Xiao F, et al. Yolact: Real-time instance segmentation. Proceedings of the IEEE/CVF international conference on computer vision. 2019: 9157-9166.
36. Redmon J, Farhadi A. Yolov3: An incremental improvement. arXiv preprint arXiv:1804.02767, 2018.

Enhancement of Mechanical and Thermal Insulation Properties of Polyvinyl Chloride Foam Using Leather Shavings

by
Chao Lei,[1,2] Weixing Xu,[1,3]* Bi Shi[1,3] and Yunhang Zeng[1,3]*
[1]*National Engineering Laboratory for Clean Technology of Leather Manufacture*, *Sichuan University*, Chengdu 610065, China
[2]*College of Biomass Science and Engineering*, *Sichuan University*, Chengdu 610065, China
[3]*Key Laboratory of Leather Chemistry and Engineering (Sichuan University)*, *Ministry of Education*, Chengdu 610065, China

Abstract

The global production of leather shavings (LSs) amounts to millions of tons annually, posing significant challenges in terms of resource waste and environmental pollution if not effectively managed. This study explores the utilization of LSs by fabricating modified leather fibers (MLFs) as reinforcing fillers to enhance the mechanical and thermal insulation properties of polyvinyl chloride (PVC) foams. The process involved pulverizing LSs and modifying them with a polyethylene glycol–isophorone diisocyanate (PEG–IPDI) prepolymer to create MLF. This MLF was then incorporated into PVC to produce MLF/PVC foam. The PEG–IPDI prepolymer modification aligned the surface free energy of MLF (33.82 ± 1.97 mJ/m^2) with that of PVC (31.08 ± 3.65 mJ/m^2), thereby improving their interfacial compatibility and imparting thermal energy storage capacity to the MLF. The resulting MLF/PVC foam exhibited enhancements in compressive strength and modulus, showing increases of 93.7% and 165.8%, respectively, compared to pure PVC foam. Furthermore, MLF/PVC foam demonstrated a slower surface temperature increase when heated using a heating plate at 110°C compared to pure PVC foam. These findings indicate that MLF enhances the mechanical and thermal insulation properties of PVC foams, primarily due to the improved foaming and thermal storage capacities imparted by the MLF.

Introduction

The leather industry significantly contributes to the global economy, with its trade value estimated at approximately $400 billion annually.[1] However, it also generates millions of tons of leather shavings (LSs) worldwide each year. These LSs can lead to substantial resource waste and environmental pollution if not treated properly.[2-3] Currently, LSs are primarily utilized for extracting collagen and its hydrolysate, or for producing adsorbents,[4] conductive materials,[5] and reinforcing fillers.[6-9] These applications often involve simple processing methods. LSs are rich in leather fibers (LFs) that have a multidirectional and hierarchical structure from collagen fibrils to collagen fibers and further to collagen fiber bundles. This structure potentially enhances the mechanical properties of polymers.[6-9] Thus, employing LF as reinforcing fillers in polymer-based composites presents a viable approach for LS resource utilization.

Polyvinyl chloride (PVC), a widely used commercial polymer, is known for its excellent flame retardancy, chemical resistance, and affordability.[10] Specifically, foamed PVC, characterized by its lightweight nature, water resistance, and thermal insulation properties, finds applications in construction, transportation, and packaging.[11] However, linear PVC typically exhibits poor foaming capacity, primarily due to its low melt strength and viscoelasticity, which in turn affects the mechanical and thermal insulation properties of PVC foams.[12-14] Restricting the movement of PVC chains through cross-linking or filling is thought to be able to ameliorate the above defects. While filling PVC with materials such as calcium carbonate,[15] mica,[16] and graphene oxide[17] is an effective strategy to improve its foaming capacity, these fillers often fall short in improving mechanical and thermal insulation properties due to their simple structures and high thermal conductivity. In contrast, the complex structure and high porosity of LF can effectively restrict polymer chain movement while exhibiting low thermal conductivity.[6-7,18] Therefore, incorporating LF into PVC foams is expected to enhance the mechanical and thermal insulation properties of PVC foams.

As global energy efficiency standards intensify, there is a growing need for foams not only to provide thermal insulation but also to possess thermal energy storage capabilities to further conserve energy.[19] Phase change materials (PCMs) are pivotal in this context, as they can store or release substantial energy during their phase transition processes.[20] Integrating PCMs with foams has been shown to enhance the thermal insulation performance of the foams.[21] Among various PCMs, polyethylene glycol (PEG) is a notable solid–liquid PCM, recognized for its high latent heat, chemical stability, and thermal robustness. However, PEG is prone to leak during the phase change process and results in adverse effects on the surrounding environment.[22] A promising

*Corresponding author E-mail address: xuwx@scu.edu.cn (Weixing Xu), zengyunhang@scu.edu.cn (Yunhang Zeng).
Manuscript received January 29, 2024, accepted for publication February 27, 2024.

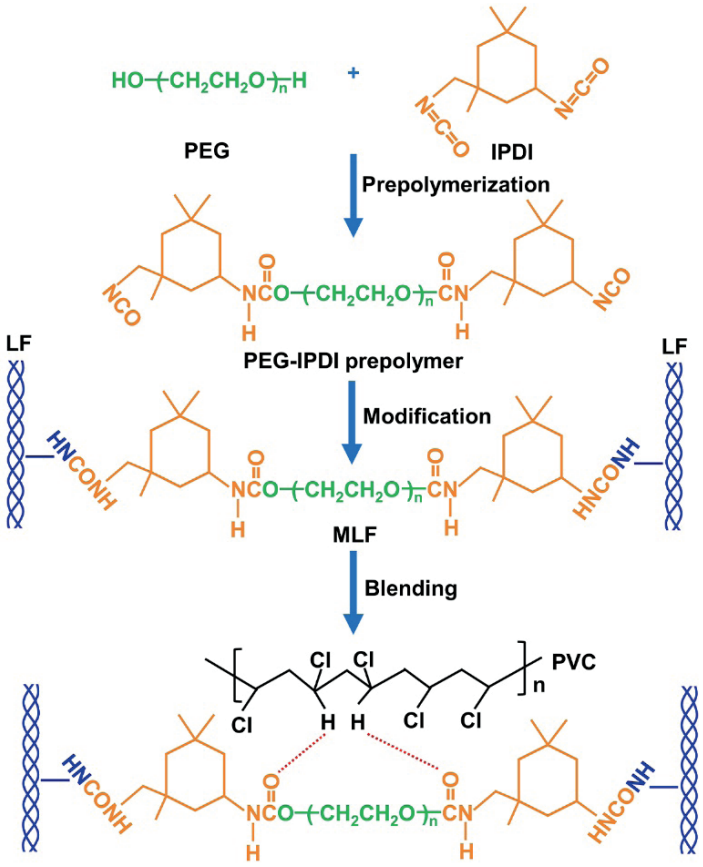

Figure 1. Schematic for the preparation of MLF and MLF/PVC foam.

solution to this issue is the conversion of PEG into a solid–solid PCM (SSPCM) using diisocyanate as a cross-linking agent and LF as a support material, which is expected to effectively mitigate leakage concerns.[23-24]

This study aims to facilitate the resource utilization of LS by employing LF as reinforcing fillers for fabricating PVC foams with superior mechanical and thermal insulation properties. LF, rich in hydrophilic groups such as –COOH, –NH_2, and –OH, exhibits poor interfacial compatibility with hydrophobic PVC.[8] Therefore, hydrophobic isophorone diisocyanate (IPDI)-capped PEG (PEG–IPDI) was used to chemically modify LF, improve the interfacial compatibility between LF and PVC, and endow LF with thermal energy storage capacity. The resulting modified LF (MLF) was then blended with PVC and foamed to produce MLF/PVC foam (Figure 1). A comparative analysis of the mechanical and thermal insulation properties of MLF/PVC foam was conducted against those of pure PVC foam, PEG–IPDI/PVC foam, and LF/PVC foam, focusing on rheological behavior, foaming capacity, and compressive and thermal properties.

Experimental

Materials

LSs were sourced from Senlu Leather Co., Ltd., Shandong, China. PEG with an average molecular weight (M_n) of 6000 g/mol, IPDI, N,N-dimethylformamide (DMF), dibutyltin dilaurate (DBTDL), and dioctyl phthalate (DOP) were acquired from Chengdu Chron Chemical Co., Ltd., Sichuan, China, and were of analytical grade. PVC (SG-5), obtained from Tianye Co., Ltd., Xinjiang, China, was of commercial quality. Barium stearate, cadmium stearate, Ca/Zn stabilizer, calcium stearate, polyethylene wax, and azodicarbonamide (AC) blowing agent, all commercial grade, were purchased from Winner New Material Technology Co., Ltd., Guangdong, China.

Preparation of MLF

Initially, the LS was thoroughly washed and neutralized to a pH of 7.0–8.0. After adequate dehydration and drying, it was pulverized using an ultra-centrifugal mill (ZM 200, Retsch, Germany) to produce LF with a size smaller than 40 mesh.

PEG was pre-dried under vacuum at 120°C for 2 h. In separate containers, 30 g (0.005 mol) of PEG and 2.225 g (0.01 mol) of IPDI were dissolved in DMF. The PEG solution was gradually added to the IPDI solution under stirring, followed by the addition of 1–2 drops of DBTDL as a catalyst. The reaction was conducted in a thermostatic oil bath at 60°C under a nitrogen atmosphere for 5 h, resulting in the formation of PEG–IPDI prepolymer with terminal isocyanate groups. Subsequently, 10 g of LF was incorporated into this prepolymer mixture and thoroughly blended. The combined mixture was then transferred to a vacuum oven and maintained at 60°C for 24 h to ensure complete cross-linking of the prepolymer with the LF. The resultant material was ground to achieve MLF of less than 40 mesh size. The grafting ratio of PEG–IPDI prepolymer to MLF was calculated using Equation (1):

$$\text{Grafting ratio} = (w_1 - w_0) \times 100/w_0, \quad (1)$$

where w_1 and w_0 represent the weights of LF before and after grafting with the PEG–IPDI prepolymer, respectively.

Preparation of PVC-based composite foams

The MLF, PVC, and various additives were homogeneously mixed using a high-speed mixer for 10 min, following the formulation presented in Table I. The blends were then melt-blended in a torque rheometer (RM-200C, Harp, China) at 135°C for 10 min. The MLF/PVC composite was subsequently hot-pressed at 150°C and 10 MPa for 10 min and foamed at 180°C for 5 min to produce the MLF/PVC foam. Control samples of PEG–IPDI/PVC foam and LF/PVC foam were prepared using an identical process, but MLF was substituted with PEG–IPDI prepolymer and LF, respectively.

Table I

Formulation of pure PVC and composite foams

Sample	Filler (per hundred/resin)	PVC (per hundred/resin)	Additives (per hundred/resin) [a]
PVC	0	100	21.3
PEG-IPDI/PVC	51.5 [b]	100	21.3
LF/PVC	25	100	21.3
MLF/PVC	25	100	21.3

[a] The additives comprised DOP (10 per hundred/resin), barium stearate (0.6 per hundred/resin), cadmium stearate (0.4 per hundred/resin), Ca/Zn stabilizer (6 per hundred/resin), calcium stearate (1 per hundred/resin), polyethylene wax (0.8 per hundred/resin), and AC blowing agent (2.5 per hundred/resin).

[b] The quantity of PEG–IPDI prepolymer in the PEG–IPDI/PVC foam corresponds to the amount grafted onto LF in the MLF/PVC foam.

Analyses of morphology and chemical structure

Morphological examination of the samples was observed using a scanning electron microscope (SEM; Apreo S HiVoc, FEI, USA). The chemical structures of the samples were analyzed using a Fourier transform infrared spectroscopy (FTIR; Nicolet iS 10, Thermo Fisher, USA). The binding energies of the elements on the sample surfaces were measured using an X-ray photoelectron spectroscopy (XPS; Thermo 250Xi, Thermo Scientific, USA). The contact angles of the samples were determined using a contact angle goniometer (DSA30, Krüss, Germany).

Analysis of rheological behavior

The rheological behavior of the samples was evaluated in an oscillatory mode using a rotational rheometer (MCR302, Anton Paar, Austria) equipped with a parallel-plate geometry (diameter = 25 mm, gap = 1 mm). Viscoelastic parameters were assessed through dynamic frequency scanning (0.01–100 rad/s) at 180 °C, maintaining a constant strain of 1% to ensure the linear viscoelastic range.

Analysis of foaming capacity

The mass densities of the samples were measured via the water displacement method, adhering to the ASTM D792-00 standard. The expansion ratio (*Φ)* was calculated using Equation (2):

$$\Phi = \rho_s/\rho_f, \quad (2)$$

where ρ_s and ρ_f represent the densities of the unfoamed and foamed samples, respectively. Pore diameter distributions were measured at 25°C using an automatic mercury intrusion porosimeter.

Testing of compressive properties

The compressive properties of the samples were tested using a universal testing machine (5967, INSTRON, USA), following the ASTM D695-02 standard.

Analysis of thermal energy storage capacity

The thermal energy storage capacities of the samples were evaluated using differential scanning calorimetry (DSC; DSC 204-F1, Netzsch, Germany). Each sample was subjected to a heating phase from 0°C to 80°C at a rate of 10°C/min, followed by cooling back to 0°C at the same rate.

The thermal reliability of the samples was assessed through an accelerated thermal cycling test. This involved repeatedly heating and cooling the samples between 20°C and 80°C for 100 and 200 cycles at a rate of 10°C/min. Post-cycling, the thermal properties of the samples were reanalyzed using DSC.

Testing of thermal insulation property

The thermal insulation performance of the samples was quantified by measuring their thermal conductivity. This measurement was performed using a transient plane source hot-disk thermal constants analyzer (TPS 2500 S, Hot Disk, Sweden). The samples were positioned on a heating plate set at 110°C, and infrared thermal imaging was conducted using an infrared imaging camera (T540, FLIR, USA).

Results and Discussion

Structure and properties of MLF

The primary objective of this research was to utilize the multidirectional and hierarchical structure of LF to enhance the mechanical and thermal insulation properties of PVC foams. The morphologies of LF and MLF were observed using SEM, as depicted in Figure 2a. The MLF retained a hierarchical structure similar to that of LF, ranging from collagen fibrils (50–200 nm) to collagen fibers (2–10 μm) and further to collagen fiber bundles (20–100 μm). This observation indicates that the unique structure of LF was preserved in MLF following modification with PEG–IPDI prepolymer.

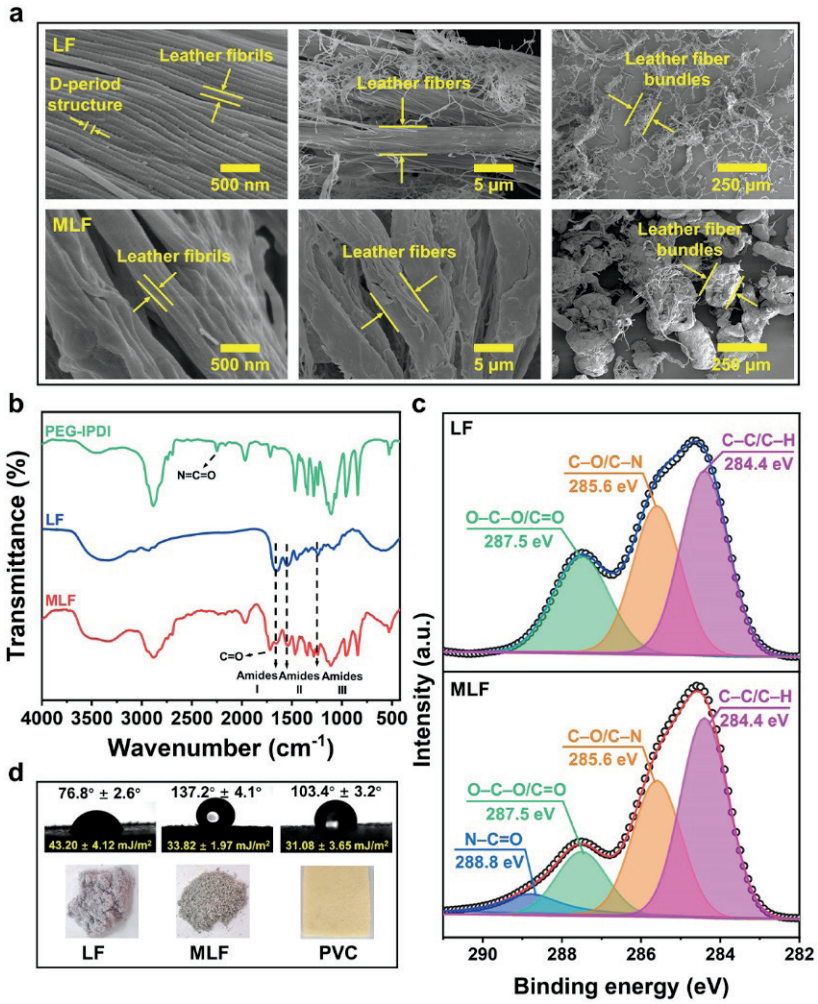

Figure 2. **(a)** SEM images; **(b)** FTIR spectra; **(c)** XPS C1s spectra; **(d)** water contact angles, surface free energies, and digital photos of LF and MLF.

The impact of PEG–IPDI prepolymer modification on MLF's chemical structure was analyzed using FTIR and XPS. Figure 2b shows the FTIR spectra of PEG–IPDI, LF, and MLF. The spectra of LF and MLF exhibited characteristic absorption peaks at 1655–1657, 1540–1544, and 1238–1242 cm^{-1}, corresponding to amides I, II, and III,[6,25-26] respectively, suggesting that the polypeptide chain structure of LF remained unaltered after modification. In the MLF spectrum, the disappearance of the N=C=O group's characteristic absorption peak at 2250 cm^{-1} (from PEG–IPDI) indicates a successful cross-linking reaction of the N=C=O groups of PEG–IPDI prepolymer with the $-NH_2$ groups of LF (Figure 1).[27] The peak at 1720 cm^{-1} in the MLF spectrum is attributed to the C=O stretching vibration of the PEG–IPDI prepolymer. The XPS analysis of the MLF surface, as shown in Figure 2c, reveals distinct features. The C1s spectrum of LF was decomposed and fitted into three peaks, centered at 284.4, 285.6, and 287.6 eV, corresponding to C–C/C–H, C–O/C–N, and O–C–O/C=O, respectively.[28] Following the modification of LF with PEG–IPDI prepolymer, the C1s spectrum of MLF shows four peaks: C–C/C–H (284.4 eV), C–O/C–N (285.6 eV), O–C–O/C=O (287.1 eV), and N–C=O (288.8 eV).[29] The appearance of N–C=O bonds in the MLF spectrum further confirms the successful grafting of PEG–IPDI prepolymer onto LF (Figure 1).

Water contact angles and surface free energies of LF, MLF, and PVC are presented in Figure 2d. The water contact angle of MLF increased to 137.2° ± 4.1°, compared to LF's 76.8° ± 2.6°, and approached that of PVC (103.4° ± 3.2°). Moreover, MLF's surface free energy (33.82 ± 1.97 mJ/m^2) was more aligned with PVC's (31.08 ± 3.65 mJ/m^2). These results suggest that the PEG–IPDI prepolymer effectively enhances the interfacial compatibility between LF and PVC, adhering to the principle of "like-dissolves-like."[30]

Interfacial structure of MLF/PVC

Effective interfacial compatibility between MLF and PVC is crucial for securing the mechanical and thermal insulation properties of MLF/PVC. The freeze-fractured surfaces of LF/PVC and MLF/PVC before foaming were observed using SEM to visually evaluate the interfacial compatibility between fillers and PVC. Figure 3a reveals noticeable gaps (highlighted with yellow circles) between LF and PVC, potentially hindering stress transfer between LF and PVC and preventing LF/PVC from fully utilizing LF's structural benefits. In contrast, minimal gaps were observed in the MLF/PVC composite, which can be attributed to the enhanced interfacial compatibility imparted by the PEG–IPDI prepolymer.

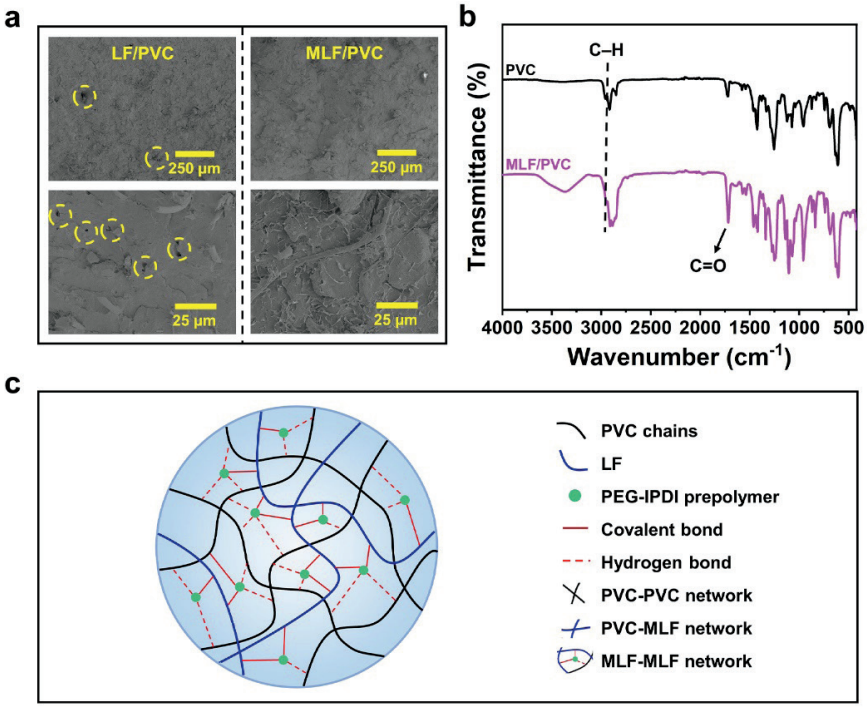

Figure 3. **(a)** SEM images of the surfaces of LF/PVC and MLF/PVC; **(b)** FTIR spectra of pure PVC and MLF/PVC; **(c)** schematic of the interaction between MLF and PVC.

The interfacial chemical structure of MLF/PVC was further analyzed by comparing the FTIR spectra of pure PVC and MLF/PVC. The FTIR spectrum of the MLF/PVC composite encompasses characteristic peaks of both MLF and pure PVC (Figures 2b and 3b). Notably, the C=O peak at 1716 cm^{-1} and the C–H peak at 2959 cm^{-1} in the MLF/PVC spectrum were shifted to lower wavenumbers compared to the C=O peak at 1720 cm^{-1} in MLF and the C–H peaks at 2952 cm^{-1} in pure PVC.[31-32] This shift suggests the possible formation of hydrogen bonds between the –NHCOO– groups of MLF and the C–H groups of PVC (Figure 1),[33] indicating that PEG–IPDI prepolymer enhances interfacial compatibility between MLF and PVC by forming interactions between MLF and PVC (Figure 3c). Improved interfacial compatibility between MLF and PVC is expected to more effectively utilize LF's structural advantages and enhance PVC's foaming capacity.

Rheological behavior of MLF/PVC

The rheological behavior of polymers is closely related to their melt strength and viscoelasticity, which is an important factor affecting their foaming capacity.[34] The variations in complex viscosity (η*), storage modulus (G′), loss modulus (G″), and loss tangent (tan δ) across dynamic frequencies for pure PVC and its composites are depicted in Figure 4. The η^* values of the four samples decreased with the increase in dynamic frequency, exhibiting the shear-thinning behavior of PVC melt (Figure 4a).[35] Pure PVC exhibited a lower η* value owing to weaker interactions among its chains, suggesting limited melt strength at the macroscopic level and, consequently, reduced foaming capacity. In contrast, PVC composites showed higher η^* values than pure PVC, attributable to the formation of various networks (PVC–PVC network, PVC–filler network, and filler–filler network) that impeded the movement of PVC chains (Figure 4a).[36] Notably, the η^* value of MLF/PVC was higher than that of LF/PVC (Figure 4a); this indicated that the more stable networks of MLF/PVC resisted the movement of the PVC chains more effectively compared to LF/PVC, thus greatly enhanced the strength of the PVC melt.[37]

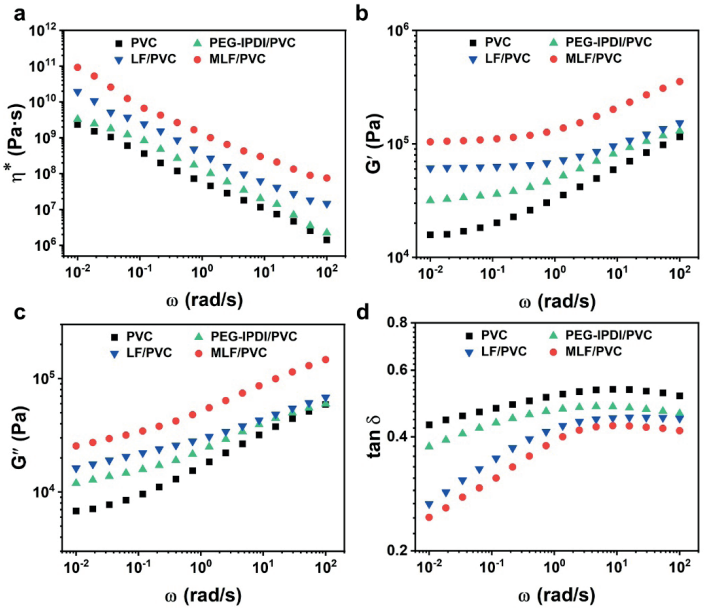

Figure 4. **(a)** Rheological behavior of pure PVC and composites: complex viscosity (η^*), **(b)** storage modulus (G′), **(c)** loss modulus (G″), and **(d)** loss tangent (tan δ).

G′ and G″ represent the energy stored and dissipated during deformation, respectively, and are crucial in determining the foaming behavior of PVC.[38] The G′ and G″ values of the samples were observed to follow the order MLF/PVC > LF/PVC > PEG–IPDI/PVC > pure PVC (Figure 4b and 4c). The order indicated that MLF/PVC had the highest elastic and viscous responses among the four samples. The loss tangent (tan δ = G″/G′) serves as an essential parameter for assessing polymer viscoelasticity.[38] The tan δ values of MLF/PVC exhibited the lowest value (Figure 4d), suggesting its superior viscoelasticity. In summary, MLF's multidirectional and hierarchical structure enhances the strength and viscoelasticity of PVC melt. This enhancement in melt strength and viscoelasticity is also expected to improve PVC's foaming capacity.

Foaming capacity of MLF/PVC

Foaming experiments were conducted on pure PVC, PEG–IPDI/PVC, LF/PVC, and MLF/PVC at 180°C for 5 min. To evaluate the influence of MLF on the foaming capacity of PVC, the microstructures and expansion ratios of the samples were analyzed. Figure 5a revealed that pure PVC foam exhibited large cell sizes and a low cell count, attributed to the low strength and viscoelasticity of the PVC melt. The inclusion of fillers (PEG-IPDI prepolymer, LF, and MLF) led to reduced cell sizes and increased cell counts in the PVC composite foams. Figures 5b–e show the pore diameter distributions of the samples. The MLF/PVC foam demonstrated superior properties, with the highest porosity (45.9%), smallest average pore diameter (30.2 μm), and lowest density (0.5323 g/cm^3). Furthermore, the expansion ratio of MLF/PVC foam increased by

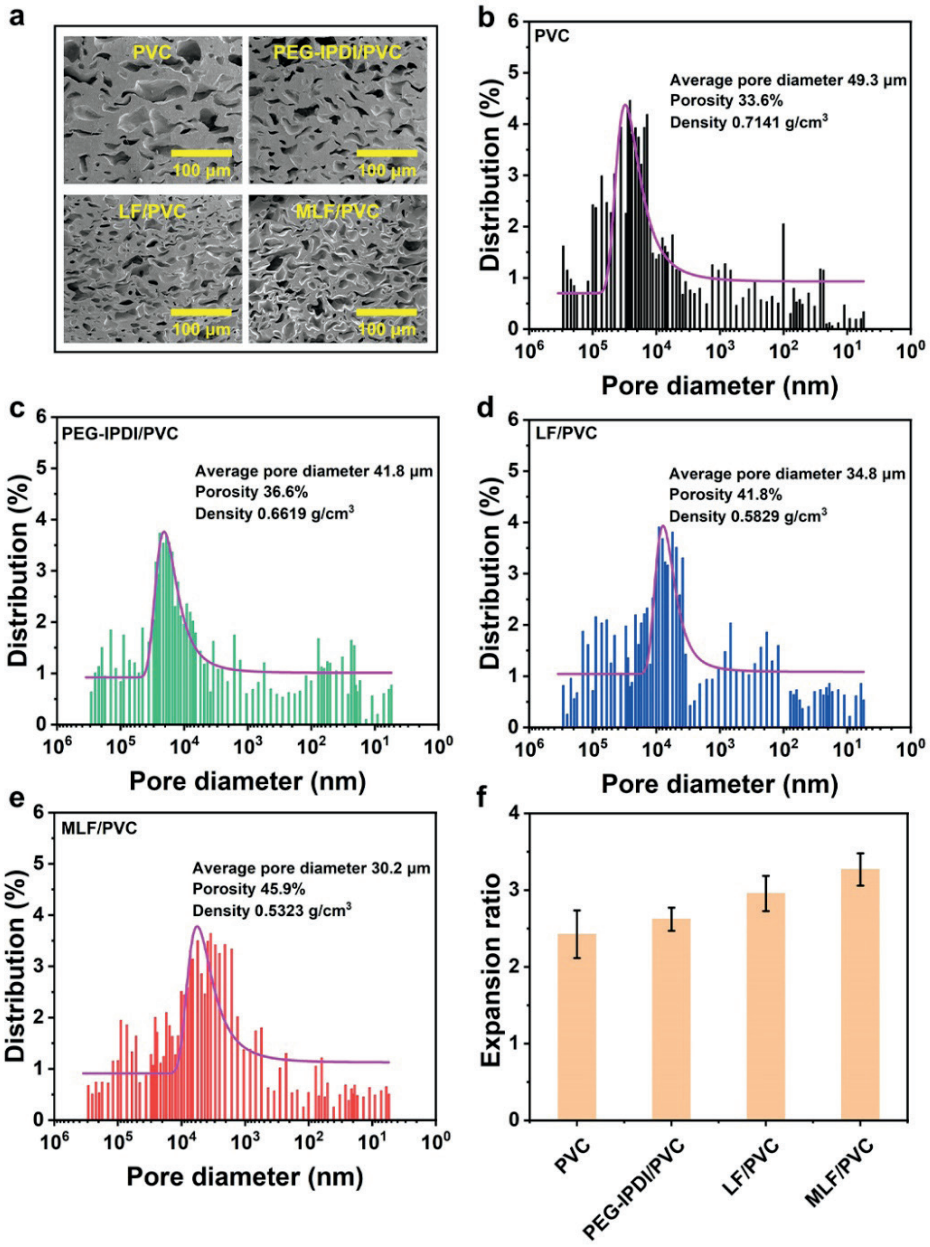

Figure 5. **(a)** Microstructures, **(b–e)** pore diameter distributions, and **(f)** expansion ratios of pure PVC and composite foams.

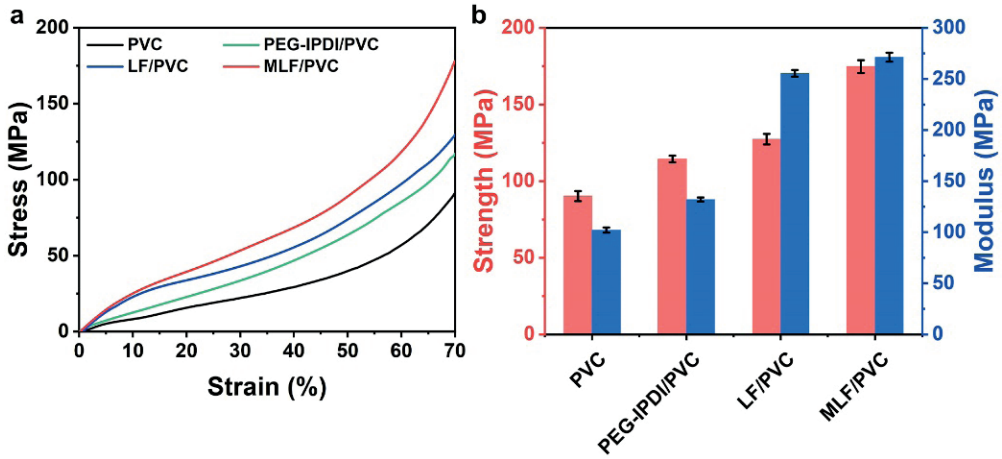

Figure 6. (a) Compressive stress–strain curves and **(b)** compressive strength and modulus of pure PVC and composite foams.

30.7% compared to that of pure PVC (Figure 5f). These findings indicate that MLF, with its multidirectional and hierarchical structure, greatly improves the foaming capacity of PVC owing to the improved strength and viscoelasticity of the PVC melt, which is expected to enhance the mechanical and thermal insulation properties of PVC foams.[12-14]

Mechanical properties of MLF/PVC foam

The compressive properties, crucial for assessing the mechanical performance of PVC foams, were evaluated.[39] Figure 6a presents the compressive stress–strain curves of pure PVC and the composite foams. All four samples exhibited no yield and maintained good ductility during compression. The ranking in terms of compressive strength and modulus was as follows: MLF/PVC foam > LF/PVC foam > PEG–IPDI/PVC foam > pure PVC foam. The compressive strength and modulus of the MLF/PVC foam were enhanced by 93.7% and 165.8%, respectively, compared to those of pure PVC foam (Figure 6b). The data indicates that MLF, with its multidirectional and hierarchical structure, enhances the mechanical properties of PVC foams. This enhancement is primarily attributed to MLF's ability to reinforce cell walls and struts. Additionally, the smaller cell size in the MLF/PVC foam contributes to a reduced bending moment in the cell walls during compressive deformation.[40]

Thermal energy storage capacity of MLF/PVC foam

The modification of LF with PEG–IPDI prepolymer transformed MLF into an SSPCM capable of thermal energy storage. Integrating MLF into PVC foam is theoretically beneficial for energy conservation and enhancing the foam's thermal insulation properties.[20-21] The thermal energy storage capacity of MLF/PVC foam was investigated by DSC analysis of the fillers and foams (Figures 7a–b), with corresponding thermal performance parameters summarized in Table II.

The DSC curves of LF showed no obvious endothermic or exothermic peaks, suggesting no phase change below 80°C (Figure 7a). However, PEG–IPDI prepolymer and MLF exhibited noticeable endothermic and exothermic peaks within the 0°–80°C range, indicating reversible thermal storage and release capabilities (Figure 7a). The phase change enthalpies (ΔH_m and ΔH_c) of MLF during melting and crystallization were lower than

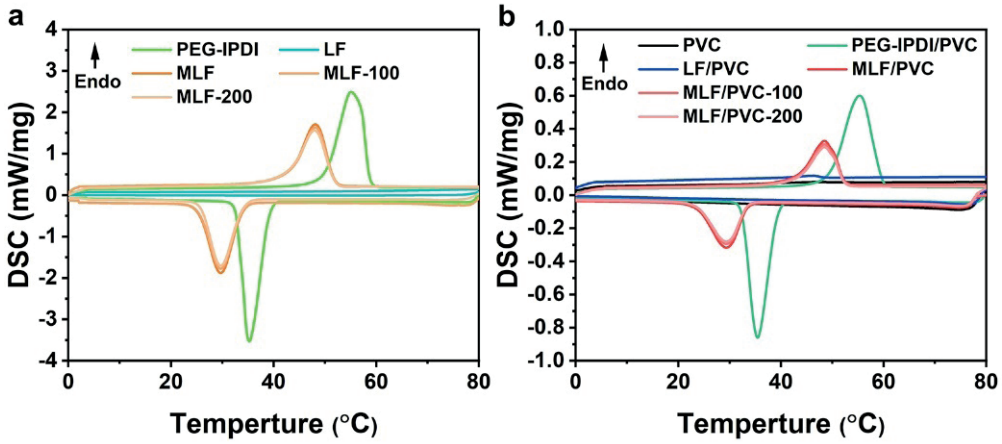

Figure 7. DSC curves of **(a)** fillers and **(b)** foams.

Table II

Thermal performance parameters of fillers and foams

	ΔH_m (J/g) [a]	T_m (°C) [a]	ΔH_c (J/g) [a]	T_c (°C) [a]
PEG-IPDI	170.1	55.2	164.2	35.2
LF	–	–	–	–
MLF	106.6	48.1	100.9	29.7
MLF-100 [b]	104.7	48.2	100.4	29.7
MLF-200 [b]	103.8	48.0	99.4	29.5
PVC	–	–	–	–
PEG-IPDI/PVC	48.6	55.0	44.3	35.3
LF/PVC	–	–	–	–
MLF/PVC	20.9	48.6	18.8	29.4
MLF/PVC-100 [b]	20.3	48.4	18.1	28.7
MLF/PVC-200 [b]	19.9	47.6	17.7	28.3

[a] ΔH_m and ΔH_c represent the phase change enthalpies during the melting and crystallization processes, respectively; T_m and T_c denote the melting and crystallization temperatures, respectively.

[b] MLF-100 and MLF-200 indicate MLF after 100 and 200 thermal cycles, respectively; MLF/PVC-100 and MLF/PVC-200 refer to MLF/PVC foam after 100 and 200 thermal cycles, respectively.

those of PEG–IPDI prepolymer (Figure 7a and Table II), suggesting a deterioration in thermal storage and release capabilities of MLF compared to those of PEG–IPDI prepolymer.[41-42] This is likely due to the cross-linked networks between LF and PEG–IPDI prepolymer restricts PEG chain movement. Despite this, the ΔH_m and ΔH_c values of MLF/PVC foam were maintained at 20.9 and 18.8 J/g, respectively, after incorporating MLF into PVC (Figure 7b), which contributes to energy savings and enhanced thermal insulation properties of the foam. Furthermore, the phase change enthalpies and temperatures for MLF and MLF/PVC foam remained relatively unchanged after 100 and 200 thermal cycles, demonstrating their excellent thermal reliability (Figure 7a and 7b and Table II).

Thermal insulation properties of MLF/PVC foam

As previously discussed, the MLF/PVC foam exhibits notable foaming and thermal energy storage capacities, which are expected to enhance its thermal insulation properties. Thermal conductivity is a critical metric for evaluating the thermal insulation properties of foams. Typically, the thermal conductivity of foams can be greatly reduced by increasing their expansion ratio.[43-44] Among the tested samples, MLF/PVC foam had the highest expansion rate, attributable to the improved foaming capacity imparted by MLF (Figure 5b). Consequently, MLF/PVC foam exhibited the lowest increase in thermal conductivity with rising temperature (25°–90°C) (Figure 8a). The thermal insulation properties were directly observed by placing samples on a heating plate at 110°C (Figure 8c), with infrared thermal images captured at different intervals (Figure 8d). MLF/PVC foam exhibited the slowest increase in surface temperature, suggesting that MLF effectively enhanced the thermal insulation properties of PVC foams by increasing their expansion rate.

Notably, the thermal conductivity of MLF (25°C, 1.7233 W/m·K) was higher than that of LF (25°C, 1.1905 W/m·K) (Figure 8b). While this might seem counterintuitive for enhancing thermal insulation, the similar thermal conductivity of MLF and PVC (25°C, 1.6951 W/m·K) allowed MLF/PVC foam to effectively utilize the thermal energy storage capacity of PEG during heat transfer. This was evidenced by the variations in thermal conductivity and surface temperature of MLF/PVC foam during the phase change interval (40°–50°C) in Figures 8a and 8c. Moreover, SEM observations of the sample cross-sections following impact fracture (Figure 8e) revealed that the multidirectional and hierarchical structure of MLF created numerous micropores and micro/nanofibrils in the cell walls. These micro/nanostructures enhance heat transfer path tortuosity and increase phonon scattering at micro/nanostructure boundaries, thereby reducing solid-phase thermal conduction.[45] In

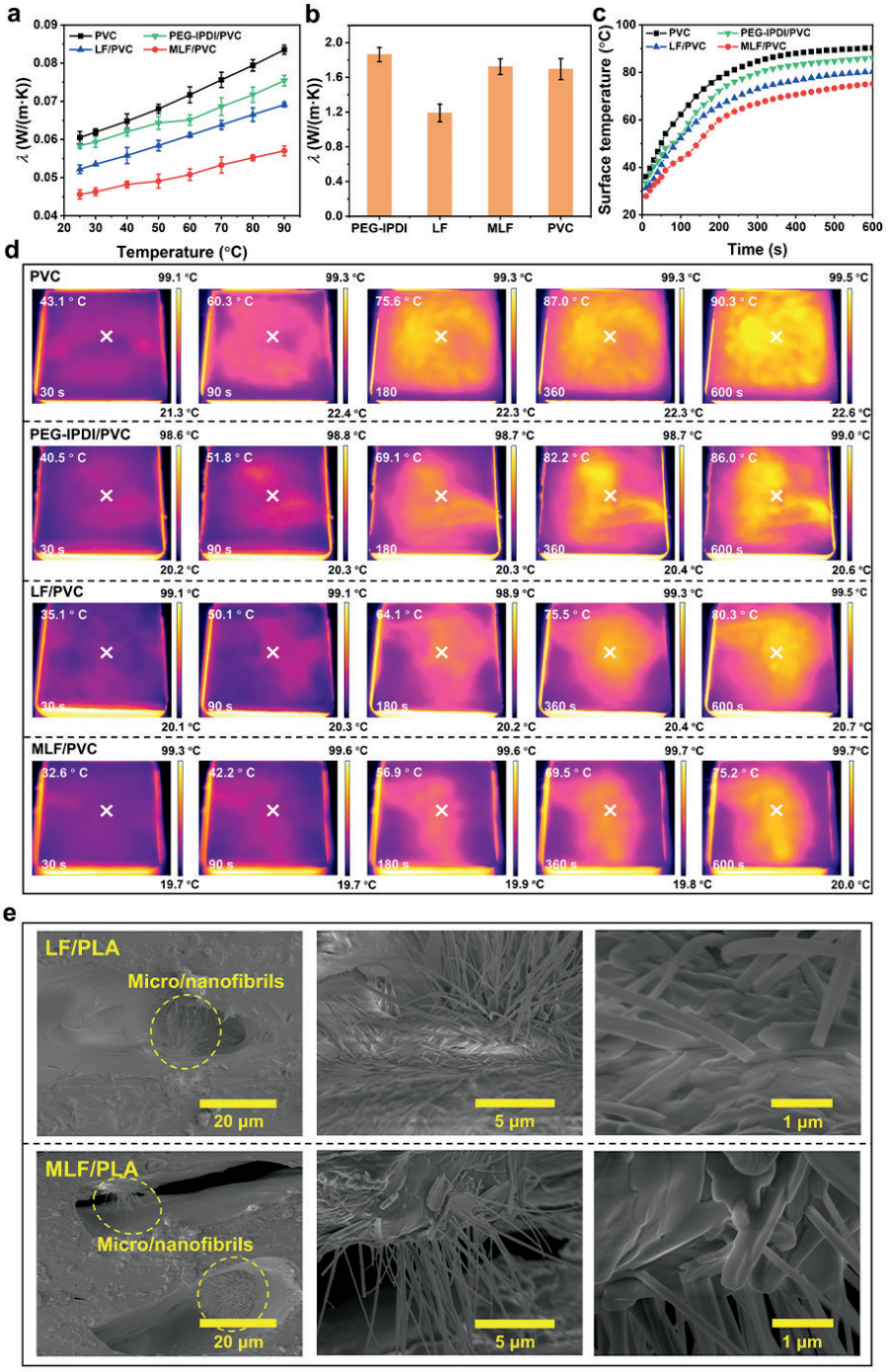

Figure 8. **(a)** Temperature-dependent thermal conductivity of pure PVC and composite foams; **(b)** thermal conductivity of fillers and PVC at 25°C; **(c)** surface temperature variations at the center point and **(d)** infrared thermal images of pure PVC and composite foams during 600 s of heating; **(e)** SEM images of the surfaces of LF/PVC and MLF/PVC foams.

summary, MLF enhances the thermal insulation properties of PVC foams through its improved foaming and thermal energy storage capacities.

Conclusion

This study demonstrated that the use of PEG–IPDI prepolymer effectively aligned the surface free energy of MLF with that of PVC, thereby enhancing their interfacial compatibility. This modification also endowed MLF with thermal energy storage capacity. Furthermore, MLF was shown to enhance the foaming capacity of PVC by increasing the melt's strength and viscoelasticity. Consequently, MLF/PVC foam exhibited a high expansion rate, small average pore diameter, and low density. These attributes collectively contributed to the notable improvement in both the mechanical and thermal insulation properties of PVC foams. The integration of MLF as a natural filler thus not only enhances the

properties of PVC foams but also presents a viable approach for the resourceful utilization of LSs. This work offers a promising direction for developing LF/PVC foam with superior mechanical and thermal insulation properties, utilizing the potential of LSs as a valuable resource.

Acknowledgement

This work was supported by the Fujian Provincial key science and technology project [2023YZ038001]. The authors acknowledge Dr. Ying Song, Dr. Xiu He, and Dr. Mi Zhou from the College of Biomass Science and Engineering of Sichuan University for their help in measurement and characterization.

References

1. Muralidharan, V., Palanivel, S., Balaraman, M.; Turning problem into possibility: A comprehensive review on leather solid waste intra-valorization attempts for leather processing. *J. Clean. Prod.* **367**, 133021, 2022.
2. Li, Y. C., Guo, R. J., Lu, W. H., Zhu, D. Y.; Research progress on resource utilization of leather solid waste. *J. Leather Sci. Eng.* **1**, 1-17, 2019.
3. Liu, J., Liu, Y. C., Brown, E. M., Ma, Z. X., Liu, C. K.; Fabrication of composite films based on chitosan and vegetable-tanned collagen fibers crosslinked with genipin. *JALCA* **116**, 345-358, 2021.
4. Peng, L. Q., Guo, L. J., Li, J. H., Zhang, W. H., Shi, B., Liao, X. P.; Rapid and highly selective removal of cesium by Prussian blue analog anchored on porous collagen fibers. *Sep. Purif. Technol.* **307**, 122858, 2023.
5. Ke, L., Zhao, K., Yan, X. Y., Cao, X. J., Wu, X. Y., Zhang, C., Luo, T. T., Ding, T., Yan, N.; Facile mineralization and valorization of Cr-containing leather shavings for electrocatalytic H_2O_2 generation and organic pollutant removal. *Chem. Eng. J.* **437**, 135036, 2022.
6. Li, S. Y., Shuai, P. Y., Wang, A. Q., Zhou, J. F., Shi, B.; Tailoring the interfacial interaction of collagen fiber/waterborne polyurethane composite via plant polyphenol for mechanically robust and breathable wearable substrate. *Compos. Part A-App. S.* **175**, 107810, 2023.
7. Xu, W. X., Wu, X. T., Shi, B.; Toughening agent for melamine formaldehyde resin: A new method for recycling chrome shavings. *Polymer* **253**, 124979, 2022.
8. Lei, C., Xu, W. X., Zeng, Y. H., Shi, B.; Study on interfacial compatibility and resilient creep resistance of silane-modified collagen fiber/polyvinyl chloride composites. *Acta Materiae Compositae Sinica* **42**, 1-12, 2023.
9. Guo, J., Dai, R., Chen, H., Liang, Y., Shan, Z. h.; Research on the composite and functional characteristics of leather fiber mixed with nitrile rubber. *J. Leather Sci. Eng.* **3**, 1-12, 2021.
10. Maou, S., Meghezzi, A., Grohens, Y., Meftah, Y., Kervoelen, A., Magueresse, A.; Effect of various chemical modifications of date palm fibers (DPFs) on the thermo-physical properties of polyvinyl chloride (PVC)–high-density polyethylene (HDPE) composites. *Ind. Crops Prod.* **171**, 113974, 2021.
11. Tang, Y., Zhang, W., Jiang, X. W., Zhao, J. Z., Xie, W. B., Chen, T.; Experimental investigations on phenomenological constitutive model of closed-cell PVC foam considering the effects of density, strain rate and anisotropy. *Compos. B Eng.* **238**, 109885, 2022.
12. Yao, K., Tan, H. Y., Lin, Y. C., Zhang, G. C., Gong, J., Qiu, J., Tang, T., Na, H., Jiang, Z. W.; Effect of polystyrene long branch chains on melt behavior and foaming performance of poly (vinyl chloride)/graphene nanocomposites. *RSC Adv.* **4**, 64053-64060, 2014.
13. You, J. A., Jiang, Z. W., Jiang, H. Q., Qiu, J., Li, M. G., Xing, H. P., Xue, J., Tang, T.; A "plasticizing-foaming-reinforcing" approach for creating thermally insulating PVC/polyurea blend foams with shape memory function. *Chem. Eng. J.* **450**, 138071, 2022.
14. Dewan, M., Adhikari, A., Chattopadhyay, D., Polyvinyl chloride foam. In Polymeric Foams: Fundamentals and Types of Foams (Volume 1), American Chemical Society, Washington, Vol. 1439, pp 237-256, 2023.
15. Khoshnoud, P., Abu-Zahra, N.; Properties of rigid polyvinyl chloride foam composites reinforced with different shape fillers. *J. Thermoplast. Compos. Mater.* **30**, 1541-1559, 2017.
16. Xu, L. F., Han, T., Li, J., Xiong, Y., Guo, S. Y.; The cell growth-induced orientation of mica in lightweight flexible poly (vinyl chloride) foams and its enhancement on sound insulation. *Compos. Sci. Technol.* **145**, 78-88, 2017.
17. Allahbakhsh, A.; PVC/rice straw/SDBS-modified graphene oxide sustainable nanocomposites: Melt mixing process and electrical insulation characteristics. *Compos. Part A-App. S.* **134**, 105902, 2020.
18. Zhang, T. R., Zeng, S. L., Jiang, H., Li, Z. S., Bai, D. Y., Li, Y. J., Li, J. J., Interfaces; Leather solid waste/poly (vinyl alcohol)/polyaniline aerogel with mechanical robustness, flame retardancy, and enhanced electromagnetic interference shielding. *ACS Appl. Mater. Interfaces* **13**, 11332-11343, 2021.
19. Villasmil, W., Fischer, L. J., Worlitschek, J.; A review and evaluation of thermal insulation materials and methods for thermal energy storage systems. *Renew. Sustain. Energy Rev.* **103**, 71-84, 2019.
20. Gao, N., Tang, T., Xiang, H. X., Zhang, W. L., Li, Y. B., Yang, C. L., Xia, T., Liu, X. L.; Preparation and structure-properties of crosslinking organic montmorillonite/polyurethane as solid-solid phase change materials for thermal energy storage. *Sol. Energy Mater. Sol. Cells* **244**, 111831, 2022.
21. Amaral, C., Pinto, S., Silva, T., Mohseni, F., Amaral, J., Amaral, V., Marques, P., Barros-Timmons, A., Vicente, R.; Development of polyurethane foam incorporating phase change material for thermal energy storage. *J. Energy Storage* **28**, 101177, 2020.
22. Zhao, Y. L., Liu, T. R., Wei, Z. K., Yuan, A. Q., Chen, Y., Jiang, L., Lei, J. X., Fu, X. W.; Polymeric phase change material networks based on multi-telechelic polyethylene glycol-derived multimer structures for thermal energy storage. *Chem. Eng. J.* **462**, 142164, 2023.
23. Xia, Y. P., Li, Q. T., Ji, R., Zhang, H. Z., Xu, F., Huang, P. R., Zou, Y. J., Chu, H. L., Lin, X. C., Sun, L. X.; Multielement synergetic effect of boron nitride and multiwalled carbon nanotubes for the fabrication of novel shape-stabilized phase-change composites with enhanced thermal conductivity. *ACS Appl. Mater. Interfaces* **12**, 41398-41409, 2020.

24. Tian, C., Ning, J. Y., Yang, Y. Y., Zeng, F. H., Huang, L., Liu, Q., Lv, J. H., Zhao, F. Q., Kong, W. B., Cai, X. F.; Super tough and stable solid–solid phase change material based on π-π stacking. *Chem. Eng. J.* **429**, 132447, 2022.
25. Li, S. Y., Wang, Y. P., Xu, S. F., Xiang, Z. W., Xu, W. X., Shi, B.; Ultradurable superhydrophobic natural rubber-based elastomer enabled by modified multiscale leather collagen fibers. *Adv. Mater. Interfaces* **7**, 2000344, 2020.
26. Lei, C., Xu, W. X., Shi, B., Zeng, Y. H.; Construction of cross-linked networks in polylactic acid biocomposites by using vegetable oil-modified collagen fibers for improving anti-stress relaxation and toughness. *Ind. Crops Prod.* **210**, 118160, 2024.
27. Wu, G., Weng, Z., Li, J. Q., Zheng, Z. C., Wen, Z. X., Fang, W. Q., Zhang, Y., Zhang, N., Chen, G., Liu, X. H.; Body armor-inspired double-wrapped binder with high energy dispersion for a stable SiO_x anode. *ACS Appl. Mater. Interfaces* **15**, 34852-34861, 2023.
28. Li, S. Y., Wang, Y. P., Xu, W. X., Shi, B.; Natural rubber-based elastomer reinforced by chemically modified multiscale leather collagen fibers with excellent toughness. *ACS Sustainable Chem. Eng.* **8**, 5091-5099, 2020.
29. Wang, C., Dong, W. J., Li, A., Atinafu, D. G., Wang, G., Lu, Y. F.; The reinforced photothermal effect of conjugated dye/graphene oxide-based phase change materials: Fluorescence resonance energy transfer and applications in solar-thermal energy storage. *Chem. Eng. J.* **428**, 130605, 2022.
30. Liu, W., Zhu, Y. F., Qian, C., Dai, H. B., Fu, Y. Q., Dong, Y. B.; Interfacial modification between glass fiber and polypropylene using a novel waterborne amphiphilic sizing agent. *Compos. B Eng.* **241**, 110029, 2022.
31. Hezma, A. M., Elashmawi, I. S., Abdelrazek, E. M., Rajeh, A., Kamal, M.; Enhancement of the thermal and mechanical properties of polyurethane/polyvinyl chloride blend by loading single walled carbon nanotubes. *Prog. Nat. Sci.: Mater. Int.* **27**, 338-343, 2017.
32. Hezma, A. M., Elashmawi, I. S., Rajeh, A., Kamal, M.; Change Spectroscopic, thermal and mechanical studies of PU/PVC blends. *Phys. B: Condens. Matter* **495**, 4-10, 2016.
33. Ali, I., Yang, W. M., Li, X. D., Ali, A., Jiao, Z. W., Xie, P. C., Dias, O. A. T., Pervaiz, M., Li, H. Y., Sain, M.; Highly electro-responsive plasticized PVC/FMWCNTs soft composites: A novel flex actuator with functional characteristics. *Eur. Polym. J.* **126**, 109556, 2020.
34. Ren, Q., Wu, M. H., Wang, L., Zheng, W. G., Hikima, Y., Semba, T., Ohshima, M.; Cellulose nanofiber reinforced poly (lactic acid) with enhanced rheology, crystallization and foaming ability. *Carbohydr. Polym.* **286**, 119320, 2022.
35. Lyu, Y., Pang, J. G., Gao, Z. J., Zhang, Q. L., Shi, X. Y.; Characterization of the compatibility of PVC/PLA blends by aid of rheological responses. *Polymer* **176**, 20-29, 2019.
36. Li, Y., Yin, D. X., Liu, W., Zhou, H. F., Zhang, Y. X., Wang, X. D.; Fabrication of biodegradable poly (lactic acid)/carbon nanotube nanocomposite foams: Significant improvement on rheological property and foamability. *Int. J. Biol. Macromol.* **163**, 1175-1186, 2020.
37. Mehrabi Mazidi, M., Edalat, A., Berahman, R., Hosseini, F. S.; Highly-toughened polylactide- (PLA-) based ternary blends with significantly enhanced glass transition and melt strength: Tailoring the interfacial interactions, phase morphology, and performance. *Macromolecules* **51**, 4298-4314, 2018.
38. Qiao, Y. H., Li, Q., Jalali, A., Yang, J. N., Wang, X. F., Zhao, N., Jiang, Y. C., Wang, S. W., Hou, J. H., Jiang, J.; In-situ microfibrillated poly (ε-caprolactone)/poly (lactic acid) composites with enhanced rheological properties, crystallization kinetics and foaming ability. *Compos. B Eng.* **208**, 108594, 2021.
39. Zhao, J. C., Wang, G. L., Wang, C. D., Park, C. B.; Ultra-lightweight, super thermal-insulation and strong PP/CNT microcellular foams. *Compos. Sci. Technol.* **191**, 108084, 2020.
40. Wang, J. C., Chai, J. L., Wang, G. L., Zhao, J. C., Zhang, D. M., Li, B., Zhao, H. B., Zhao, G. Q.; Strong and thermally insulating polylactic acid/glass fiber composite foam fabricated by supercritical carbon dioxide foaming. *Int. J. Biol. Macromol.* **138**, 144-155, 2019.
41. Alva, G., Lin, Y. X., Fang, G. Y.; Synthesis and characterization of chain-extended and branched polyurethane copolymers as form stable phase change materials for solar thermal conversion storage. *Sol. Energy Mater. Sol. Cells* **186**, 14-28, 2018.
42. Du, X. S., Qiu, J. H., Deng, S., Du, Z. L., Cheng, X., Wang, H. B.; Flame-retardant and solid-solid phase change composites based on dopamine-decorated BP nanosheets/Polyurethane for efficient solar-to-thermal energy storage. *Renewable Energy* **164**, 1-10, 2021.
43. Song, L. M., Chen, Y. Q., Gao, Q. C., Li, Z., Zhang, X. Y., Wang, H. L., Guan, L., Yu, Z. J., Zhang, R., Fan, B. B.; Low weight, low thermal conductivity, and highly efficient electromagnetic wave absorption of three-dimensional graphene/SiC-nanosheets aerogel. *Compos. Part A-App. S.* **158**, 106980, 2022.
44. Jia, L. J., Phule, A. D., Yu, Z., Zhang, X., Zhang, Z. X.; Ultra-light poly(lactic acid)/SiO_2 aerogel composite foam: A fully biodegradable and full life-cycle sustainable insulation material. *Int. J. Biol. Macromol.* **192**, 1029-1039, 2021.
45. Noroozi, M., Panahi-Sarmad, M., Abrisham, M., Amirkiai, A., Asghari, N., Golbaten-Mofrad, H., Karimpour-Motlagh, N., Goodarzi, V., Bahramian, A. R., Zahiri, B.; Nanostructure of aerogels and their applications in thermal energy insulation. *ACS Appl. Energy Mater.* **2**, 5319-5349, 2019.

Expanding the Practical Approach for Salt-Free Tanning: A Chrome-free System

by
M. Sathish,*[1] Surojit Manna[1] and Nakkala Gopi Krishna
[1]*Regional Centre, CSIR-Central Leather Research Institute*, Kolkata, India

Abstract

Our research group previously established a practical approach for salt-free chromium tanning by changing the order of addition of masking salts (COAMS) for electrolyte-cum-masking effect. The present work deals with the modified COAMS process for developing a salt-chromium-free tanning system using aluminium. The tanning conditions such as Al to masking salt (cirtate) ratio, Al_2O_3 offer, the effect of phenolic syntan, and its order of addition on tanning performance have been studied in detail. It was found that the addition of 3% sodium carbonate (based on the weight of aluminium sulfate) along with aluminium sulfate reduces the acidity without affecting the tanning performance and leather quality. The ideal conditions for the pickle-free aluminium tanning were found to be 1.5% Al_2O_3 offer, 5% phenolic syntan offer, and an Al to citrate ratio of 1:0.2. It was also found that the order of addition of phenolic syntan did not affect the tanning performance. Furthermore, in comparison to leather produced without syntan, the combined effect of aluminum and phenolic syntan raises the shrinkage temperature by 6°C (Without syntan: 74°, with syntan-80°) and decreases the rate of shrinkage by 74%. However, the addition of phenolic syntan did not improve Al exhaustion and leaching resistance to water. The physical characteristics and fiber compactness have been improved by the addition of phenolic syntan. SEX-EDAX study reveals that the aluminum is uniformly distributed throughout the cross-section.

Introduction

The discharge of total dissolved solids from the tanning process and its impact on the end-of-pipe treatment is one of the long-standing problems associated with the leather industry. For a considerable amount of time, there have been multiple attempts to reduce the Total Dissolved Solids (TDS) load in tannery wastewater. Several technological interventions such as low-salt pickling, salt-free pickling[1-2] and pickle-free tanning[3-6] processes have been implemented at commercial scale to reduce the TDS load. However, it is not widely applied due to some practical difficulties. Recently, our research team developed practical approaches for pickle-free chromium tanning[7] and the process details are given below:

(i) Salt-free Chrome Tanning in Deliming Liquor (CTDL)
In this system, the deliming is carried out at 50% float followed by H_2O_2 treatment to convert the sulfide into sulfate. After, deliming the salt concentration in deliming liquor was around 3.5% and it was sufficient to adjust the pelt pH to 5.0 without acid swelling. The pH-adjusted pelts were subjected to chromium tanning without any further treatment.

(ii) Changing the Order of Addition of Masking Salts (COAMS)
Generally, masking salts are added before the basification (i.e) after the acidification and chromium treatment to improve the precipitation point of chromium. Whereas in the COAMS process, the masking salts were added before the acidification and chromium treatment, therefore it can also act as an electrolyte that prevents the acid shock while adjusting the delimed pelt pH to 5.0.

Both approaches are simple and easy to adopt at a commercial scale. Further, the process does not involve any specialty chemicals and also reduces the consumption of acid/alkali. Therefore, the above methods are environmental/tanners-friendly and economically beneficial.

On the other hand, globally the search for chromium-free tanning systems is increasing due to the toxicity associated with chromium compounds, especially Cr(VI).

Considerable attempts have been made to develop chromium-free mineral tanning systems. Patent no PCT/NL2020/050773 deals with the modification of zeolite with acid and used as tanning agent in leather manufacturing.[8] In this method, the pickled pelt (pH: 3.0) is treated with the modified zeolite. Xinhua Liu et.al., developed a salt-free pickling and chrome-free tanning technology using epoxy-terminated hyperbranched polyamine-ester (EHBP) and aluminium (III) salt as pickling and tanning agent, respectively.[9] Madhan et al., developed the complexes of aluminium (III) & Zinc(II) using different ligand combinations such as sodium citrate, triethylenetetramine, phthalic acid, and sodium tartrate.[10] An attempt had been made to develop Zirconium-Aluminium-Titanium complex as a tanning agent and the shrinkage temperature of the leather was increased up to 95° (Patent No CN102787181A).[11] Chandrababu et al., extensively studied the use of Iron (III) as a self-tanning agent by chelating with

*Corresponding author email: sathish@clri.res.in ;Tel: 033 232926
Manuscript received February 15, 2024, accepted for publication March 12, 2024.

the suitable ligands viz. fatty acid, aliphatic/aromatic carboxylic acid to increase the stability of iron complex and also to increase the hydrothermal stability of the final leather.[12] Further, Fathima et al., developed an iron-tetrakis hydroxymethyl phosphonium sulfate (THPS)-based combination tanning and optimized the iron to THPS ratio on thermal stability of the tanned leather.[13] Further, they have also studied the influence of various ligands on the thermal stability of the final leather. US patent no 4731089 deals with the development of a mixed metal tanning system using aluminum and titanium complex masked with the salt of polyhydroxymono carboxylic acid. Recently, Zhicheng Jiang et al., employed trojan horse strategy for the development of Al-Zr-Oligosaccharides complex and used them as a tanning agent.[14]

Further to reduce the salinity in wastewater, few attempts have been made to develop pickle-free and chromium-free tanning technologies. The US patent no US 7169191 provided the process for the preparation of synthetic aluminium tanning agent by incorporating the aluminum into the formaldehyde-free polymeric matrix as a solo tanning agent for pickle-free processes.[15] Further, Patent No CN115011742 provided the process for pickle & chrome-free tanning-based epoxy-modified collagen polypeptide.[16]

It is evident from literature that limited attempts have been made to develop pickle-chromium-free tanning systems. While searching for an alternative chromium-free mineral tanning agent, aluminium is found to be a suitable material because of its low cost and availability. In this work, we have attempted to develop pickle-chromium-free tanning using aluminium with the modification of our previously established COAMS process.

Materials and Methods

Conventionally processed goat delimed pelts have been taken as raw material for tanning trials. $Al_2SO4_3.16H_2O$ and trisodium sodium citrate dihydrate were procured from M/s Merck. Commercial-grade chemicals were used for leather processing. Analytical-grade chemicals were used for analysis.

Table I

Process recipe for salt-chromium-free tanning

Raw material: Goat delimed pelts, Thickness (Neck): ~ 1.5 mm

Process/Chemicals	% Offer	Time	Remarks
Masking Salt Treatment			
Water	50		
Sodium citrate	"X"		
Sodium formate	1	30 min	
Acidification			
Formic acid	0.5		
Water	5	3*15 min+30 min	
Sulfuric acid	0.2		
Water	10	2*30 min+60 min	pH adjusted to around 5.0
Tanning			
Phenolic syntan	"Y"	30 min	
Al as Al_2O_3	"Z"		
Sodium carbonate	3*	2*60+60 min	After the complete addition aluminium pH dropped to around 3.0. Aluminium penetration was checked using pyrocatechol violet indicator
Basification			
Sodium carbonate	1.0-1.5		
Water	10	3*30 min+120 min	pH adjusted to 4.0. Drained and Piled

*% offer based on the weight of aluminium sulfate

Y – Phenolic syntan offer varied from 0 to 10 % (0, 1, 2.5, 5, 7.5 and 10%)

Z – Al_2O_3 offer varied from 1 to 3% (1, 1.5, 2, 2.5 and 3%)

Optimization of Aluminium to Masking Salt Ratio

Thirty goat delimed pelts were grouped into 6 (each group contains 5 delimed pelts), marked, and subjected to tanning process as per the recipe given in Table I. The amount of Al offer was kept constant (Al_2O_3: 1.5% w/w - Based on pelt weight) and for every mole equivalent of Al, the sodium citrate mole equivalent was varied from 0 to 0.3% w/w (0, 0.1, 0.15, 0.2, 0.25, 0.3).

Effect of Phenolic Syntan on Tanning Performance

Six groups of delimed pelts were marked (each group having 5 delimed pelts) and subjected to the tanning process as per the recipe given in Table I where the optimized Al: Sodium citrate ratio and 1.5% Al_2O_3 were offered. The amount of phenolic syntan offered (based on pelt weight) was varied from 0 to 10% w/w. The effect of phenolic syntan on aluminium exhaustion was analyzed using Inductively Coupled Plasma – Optical Emission Spectrometry (ICP-OES)

Changing the Order of Addition of Phenolic Syntan on Tanning Performance

Six groups of delimed pelts were marked (each group having 5 delimed pelts) and subjected to the tanning process (Al: Sodium citrate ratio and 1.5% Al_2O_3) where the order of addition of phenolic syntan was varied.

(i) Phenolic syntan followed by aluminium before basification

(ii) Phenolic syntan and aluminium together

(iii) Aluminium followed by syntan before basification

(iv) Aluminium followed by syntan after basification

Optimization of Al_2O_3 Offer

Five groups of delimed pelts were marked (each group having 5 delimed pelts) and subjected to the tanning process as per the recipe given in Table I. The optimized Al:Sodium citrate (1:0.2) ratio was kept constant and the amount of Al_2O_3 offer (based on pelt weight) was varied from 1.0 to 3.0% w/w (1, 1.5, 2, 2.5, 3.0). The aluminium exhaustion for different percentages of Al_2O_3 offer was estimated through Inductively Coupled Plasma – Optical Emission Spectrometry (ICP-OES).

Optimized Tanning Process

Further, ten delimed pelts were cut along the backbone, marked, and grouped separately. The left and right halves were subjected to an optimized tanning process with and without phenolic syntan treatment, respectively. After 15 days of aging, the tanned leathers were converted into crust leather as per the process recipe given in Table II.

Analysis of Aluminium Leaching

The tanned leather obtained from the optimized tanning process was aged for 48 hrs and subsequently, a specimen was taken from the official sampling position. Further, the specimen was cut into small pieces. Fifteen grams (moisture-free basis) of cut pieces were added into a conical flask containing 150 ml of double distilled water and agitated at 250 rpm. Every 1 hr time interval, the leachate was drawn from the conical flask and subjected to aluminium estimation through ICP-OES.

Hydrothermal Shrinkage Temperature Measurements

Prolific shrinkage temperature was used for the measurement of hydrothermal shrinkage temperature. The test specimens of 50*3 mm size (l*b) were cut from the samples to be tested. The jig is placed inside the beaker containing water and it has a fixed pin at its lower end and a hook at its upper end for holding the test specimen in between. The thread from which the hook is suspended passes over a lightweight aluminium pully, which also carries the circular scale. The other end of the thread has a dead weight attached to it to apply the specified tension on the test specimen. Further, the system was heated at the rate of 2°/min with constant stirring. The temperature at which the test specimen has shrunk to such an extent that moving the dial (circular scale) half a division from the initial position is noted as shrinkage temperature. Once the movement of the dial started, the division of the circular scale was noted at different time intervals to analyze the rate of shrinkage.

Physical Strength Characteristics and SEM Analysis

According to the IULTCS standard procedure, specimens for a variety of strength characteristics, including tensile strength, % elongation at break, tear strength, grain crack load, and distension at grain crack, were obtained. Before analysis, every specimen was conditioned for twenty-four hours at 25±1°C and 65% RH.[17-20] TESCAN-CLARA scanning electron microscope was employed to analyze the morphological characteristics and aluminium distribution (EDAX mapping).

Table II

Post-tanning process recipe (Thickness: 1.0 mm)

Process/Chemicals	% Offer	Time	Remarks
Wetting back			
Water	100		
Wetting agent	0.1	30 min	Drain
Neutralization			
Water	100		
Sodium Formate	1		
Sodium bicarbonate	0.7	pH: 5.0-5.2	Drain/Wash
Re-tanning			
Sulfone syntan	5.0		
Melamine syntan	4.0		
Acrylic syntan	2.0	90 min	
Fatliquoring			
Vegetable oil based fatliquor	5.0	30 min	
Synthetic fatliquor	6		
Sulfited fatliquor	4	150 min	
Fixing			
Formic acid + Water	1.5 + 5	2 × 10 min + 60 min	Drain/Wash, drying and staking

Results and Discussion

Salt-Free Aluminium Tanning – Process Strategy

The previously established COAMS process deals with the addition of masking salts before the acidification. In this process, the masking salts not only alter the charge/hydrolytic behaviour of chromium but also increase the ionic strength, and therefore the ionic imbalance of the system will be reduced. Hence, the delimed pelt pH can be reduced to the required tanning pH (5.0) without acid swelling/acid shock. A similar concept has been employed in the present work with minor modifications. In our previous study (chrome tanning) sodium acetate was used as masking salt but the present study employed tri-sodium citrate and sodium formate as masking salts. Further, it is a well-known fact that the acidity of aluminium sulfate is higher than basic chromium sulfate due to the high charge-to-size ratio. Hence there may be a possibility for the occurrence of acid swelling after adding aluminium sulfate even if the system has masking salt as an electrolyte. After conducting a series of experiments, it has been found that the addition of aluminium sulfate along with 3% sodium carbonate (% based on the weight of aluminium sulfate) reduces the aluminium acidity without affecting the tanning performance. After the complete addition of aluminium sulfate, the system's pH would be around 3.0 and it will be increased up to 4.0 at the end of tanning.

Optimization Study

In order to optimize the Al:Citrate ratio, 6 different trials were carried out and the shrinkage temperature of tanned leather was taken as the basic criteria for shortlisting an ideal ratio. The shrinkage temperature of each tanning trial is given in Table III. It is evident from Table III that the shrinkage temperature of the 1:0, 0.1, 0.15 system is around 71° whereas it has been increased up to 74° for a 1:0.2 ratio. However, it falls when the citrate equivalent is increased beyond 0.2. It may be due to the over-masking and generation of stable Al-citrate complex. Hence, the 1:0.2 ratio has been optimized. It is well established that the combination of aluminium with plant polyphenols improves the tanning performance as well as quality of the final leather. However, the wattle-aluminium complex imparts ash color to the tanned leather. This work mainly focuses on understanding the effect of phenolic syntan offer and its order of addition on the tanning performance. The Al: Citrate ratio and Al_2O_3 offer is 1:0.2 & 1.5%, respectively. It is evident from Figure 2 that no change in shrinkage temperature for 0, 1% phenolic syntan offer (74°), and a minor change in 2.5% offer

(75°). However, a considerable increase in shrinkage temperature has been observed for 5% (80°) and it remains unaltered for 7.5% and 10%. Therefore, 5% phenolic syntan offer would be an ideal offer. On the other hand, it was found that the order addition of phenolic syntan does not affect shrinkage temperature and other tanning characteristics.

Subsequently, tanning trials have been carried out with the optimized ratio (Al:Cittrate – 1:0.2, Phenolic syntan – 5%) where the Al_2O_3 offer has been varied from 1 to 3.0%. Further, two sets of trials have been carried out with and without phenolic syntan. The shrinkage temperature and aluminium exhaustion is given in Table III. In the case of without phenolic syntan treatment

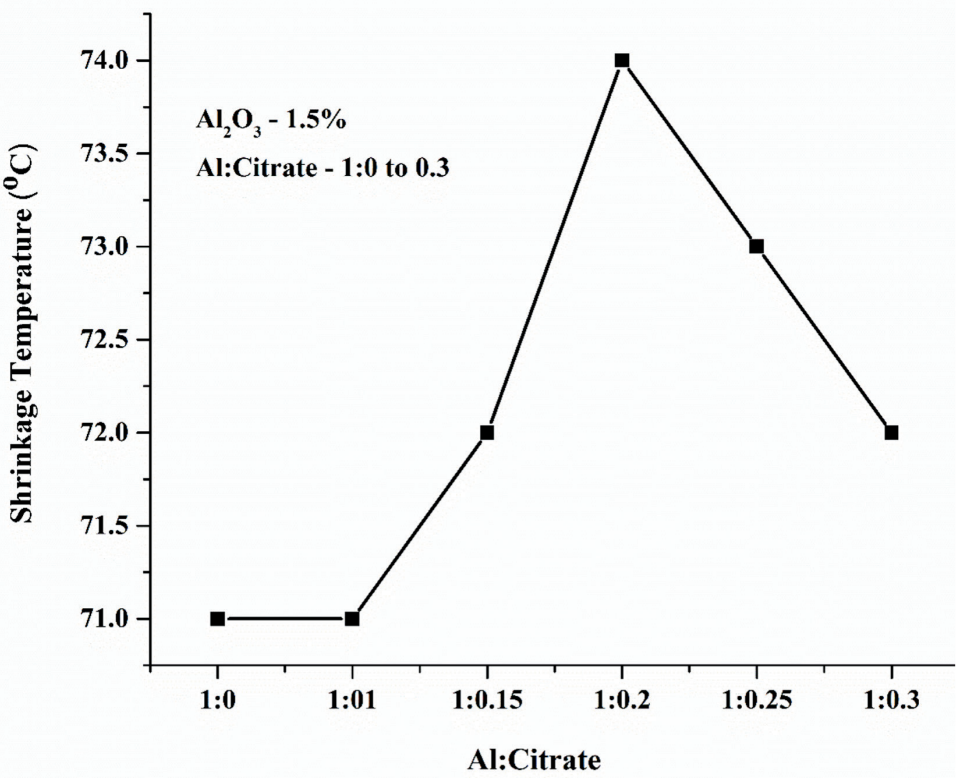

Figure 1. Optimization of Al:Citrate ratio

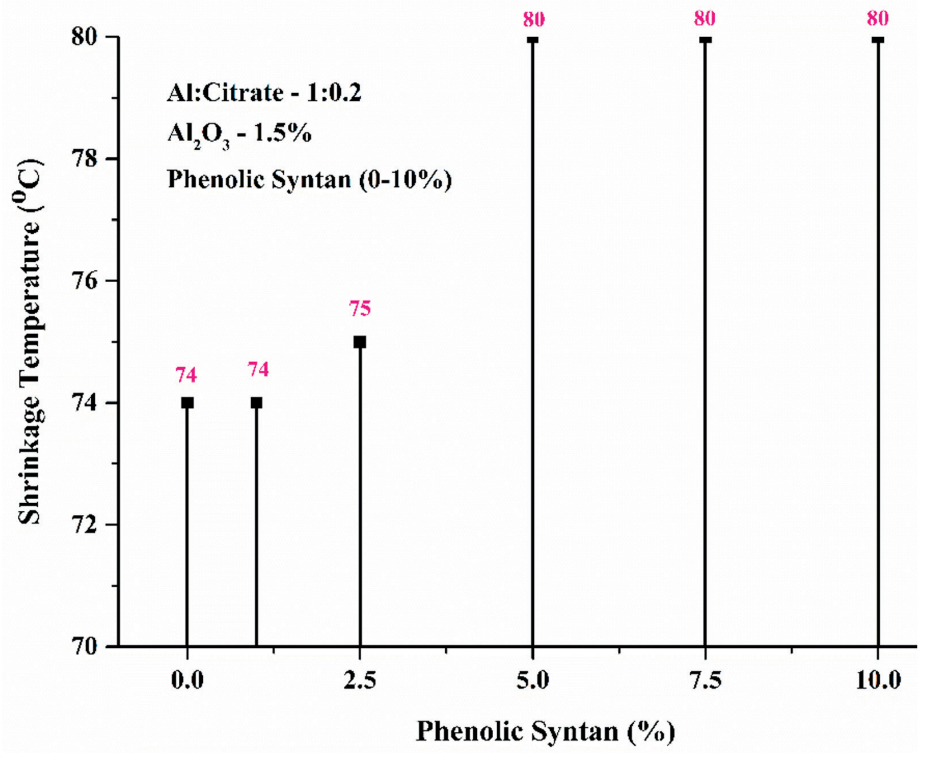

Figure 2. Optimization of phenolic syntan offer

Table III

Optimization of Al_2O_3 offer

Al: Citrate	Al_2O_3 Offer (%)	0% Phenolic syntan		5% Phenolic syntan	
		Shrinkage Temperature (°C)	Al exhaustion (%)	Shrinkage Temperature (°C)	Al exhaustion (%)
1:0.2	1.0	71±1	76	76±1	77
	1.5	74±1	81	80±1	81
	2.0	74±1	83	80±1	84
	2.5	74±1	75	80±1	76
	3.0	76±1	70	82±1	72

the shrinkage temperature of 1% Al_2O_3 offered leather was 71° whereas it was 74° for 1.5 to 2.5% and further, it was increased to 76° for 3.0%.

On the other hand, the aluminium exhaustion for 1% system was 76% and subsequently increased to 81% and 83% for 1.5% & 2.0%, respectively. It is also clear from Table III that the Al uptake falls when the offer increases to 2.5 and 3%. Similarly, it was found that the addition of phenolic syntan increased the shrinkage temperature and also a marginal increase in exhaustion has been observed. For 1% and 1.5% offer, shrinkage temperature is 76° and 80°, respectively. Further, it remains unaltered for 2.0 & 2.5% and a marginal increment has been observed for 3.0%. The exhaustion pattern of tanning trials with and without phenolic syntan is almost similar. Hence, it can be concluded from the study that the optimized tanning conditions are (i) Al:Citrate – 1:0.2 (ii) Phenolic syntan offer– 5% (iii) Al_2O_3 offer – 1.5% (iv) Order of addition – any place after acidification.

Leaching Study

It is a well-known fact that aluminium-tanned leather has poor resistivity against water leaching due to the formation of labile complexes with protein carboxyl groups. In order to understand the effect of phenolic syntan on the leachability of aluminium, the matched pair of tanned leather obtained from the optimized tanning process has been subjected to water leaching. The leachability of aluminium at different time intervals is shown in Figure 3. It is evident from the Figure that the leachability pattern

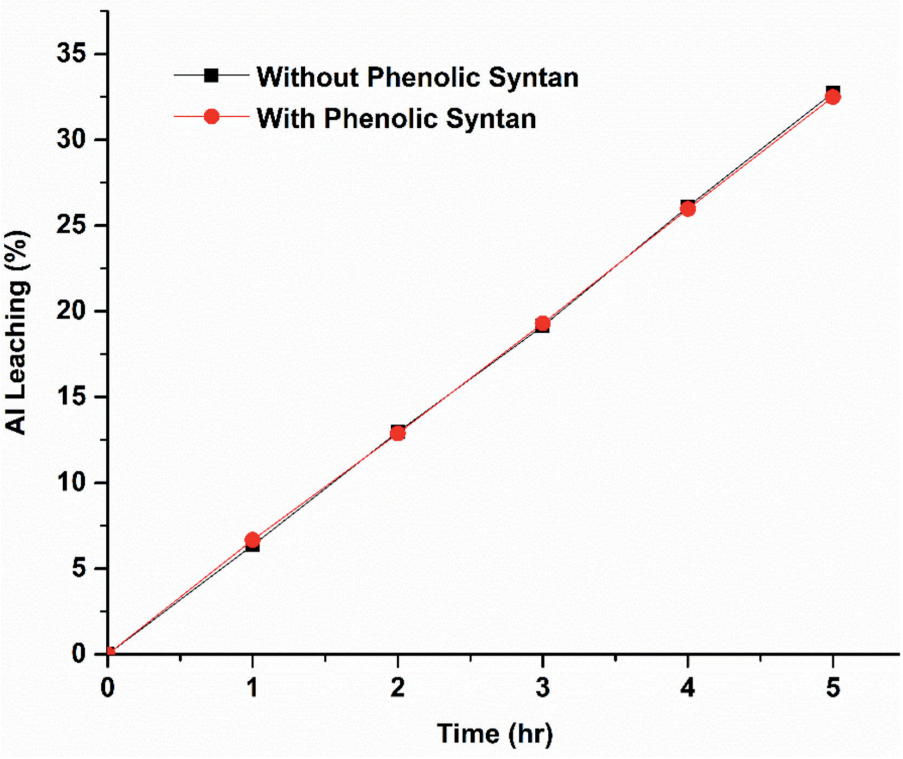

Figure 3. Effect of phenolic syntan on A1 leaching

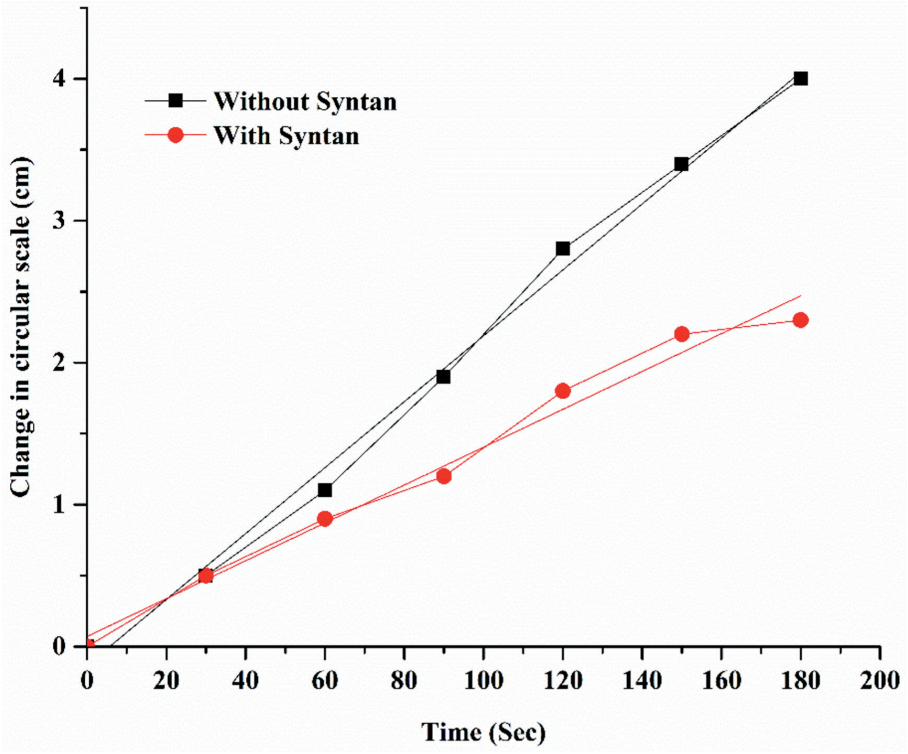

Figure 4. Rate of hydrothermal shrinkage

of leather treated with syntan and without syntan is similar and no considerable difference has been observed. It was also observed that around 6-7% of aluminium is leached out for every 1 hr time interval. After 5 hrs around 32% of the aluminium is leached out. From this experiment, it can be concluded that the addition of phenolic syntan is not reducing the aluminium leaching.

Rate of Hydrothermal Shrinkage

It is understood from the previous experiments that the addition of phenolic syntan increases the hydrothermal shrinkage temperature. Further, in order to understand the effect of phenolic syntan on the rate of leather shrinkage, the change in the circular scale division due to the contraction of the test specimen as a function of time has been monitored (refer to method for further details). It is evident from Figure 4 that the shrinkage pattern obeys the liner model. The correlation co-efficient (R^2) value of without and with syntan-treated leather is 0.99325 and 0.98043, respectively. Further, the corresponding slope value can be correlated with the rate of shrinkage (higher the slope, faster the shrinkage). The slope value of leather from without syntan treatment is 0.0232 whereas it is 0.0133 for syntan treated leather. Hence, the shrinkage rate of leather processed without syntan treatment is 74% faster than the syntan-treated leather.

Further, it is also evident from Figure 4 that the leather without syntan treatment reached the final division (4 cm) of the circular scale within 180 seconds whereas syntan-treated leather reached only about 2.3 cm within 180 seconds. These results demonstrate that the syntan-treated leather has better hydrothermal resistance and also a slow shrinkage pattern. This may be due to the synergetic effect of aluminium and phenolic syntan and also the formation of a multipoint network.

Physical Strength Characteristics

The physical strength characteristics of the crust leathers (with and without syntan) have been analyzed and results are given in Table IV. Further, the variations in strength characteristics with respect to the without syntan system are shown in Figure 5. The tensile strength of syntan-treated leather is 23% higher than the without syntan system and also a 7% reduction in elongation at break. Similarly, 4%, 7%, and 3% increase in tear strength, load at grain crack and distension at grain crack, respectively. Further, 10% reduction has been observed for water vapor permeability. The reduction in elongation and water vapor permeability indicates the compactness of the syntan treated system.

SEM Analysis

The distribution of Al in the crust leather has been mapped using EADX analysis and the same is shown in Figure 6. It is evident from the Figure that the Al is distributed uniformly throughout the cross-section. Further, the aluminium to the sulfur ratio is also similar for both syntan-treated and non-syntan systems. Further, the cross-sectional view of the crust obtained from both systems is shown in Figure 7. It is evident that the fiber structure of the syntan-treated leather is more compact and cemented than the without syntan system, Further, it is also observed that the fiber splitting of the syntan-treated leather was good when compared to the non-syntan system.

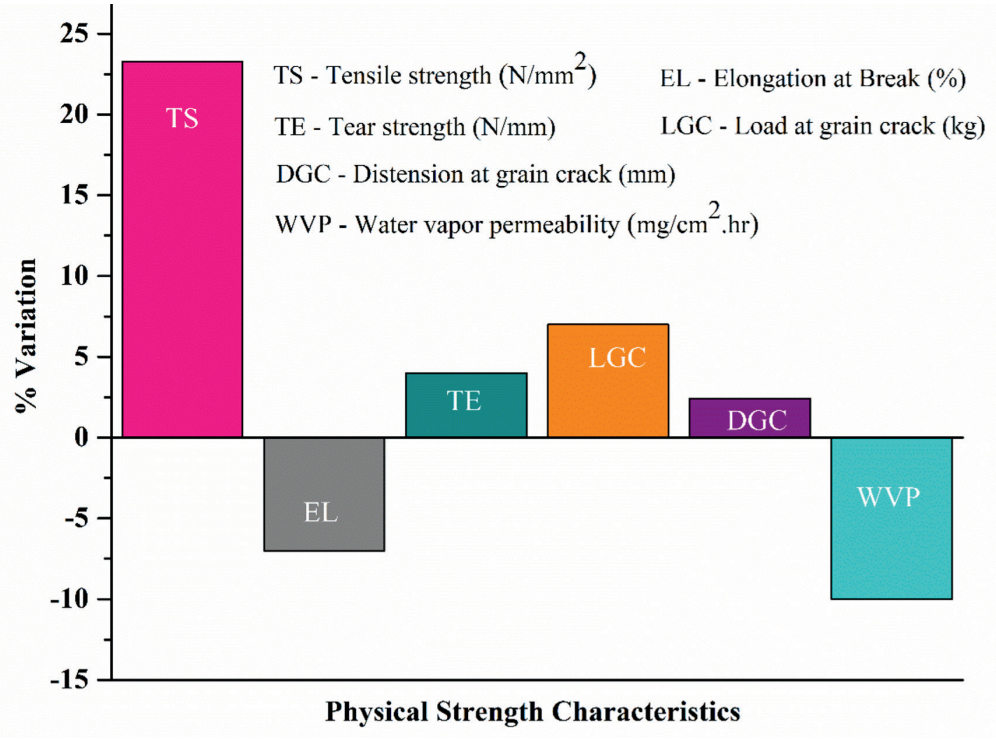

Figure 5. Rate of hydrothermal shrinkage

Table IV

Physical strength characteristics of salt-free aluminium tanned leather with and without syntan treatment

Physical Strength Characteristics	Without Syntan	With Syntan
Tensile Strength (N/mm2)	23.04	28.4
Elongation at Break (%)	65.2	60.7
Tear Strength – N/mm	106	110
Load at Grain Crack (kg)	28.1	30
Distension at grain crack (mm)	8.3	8.5
Water vapor Permeability (mg/cm^2.hr)	3.7	3.33

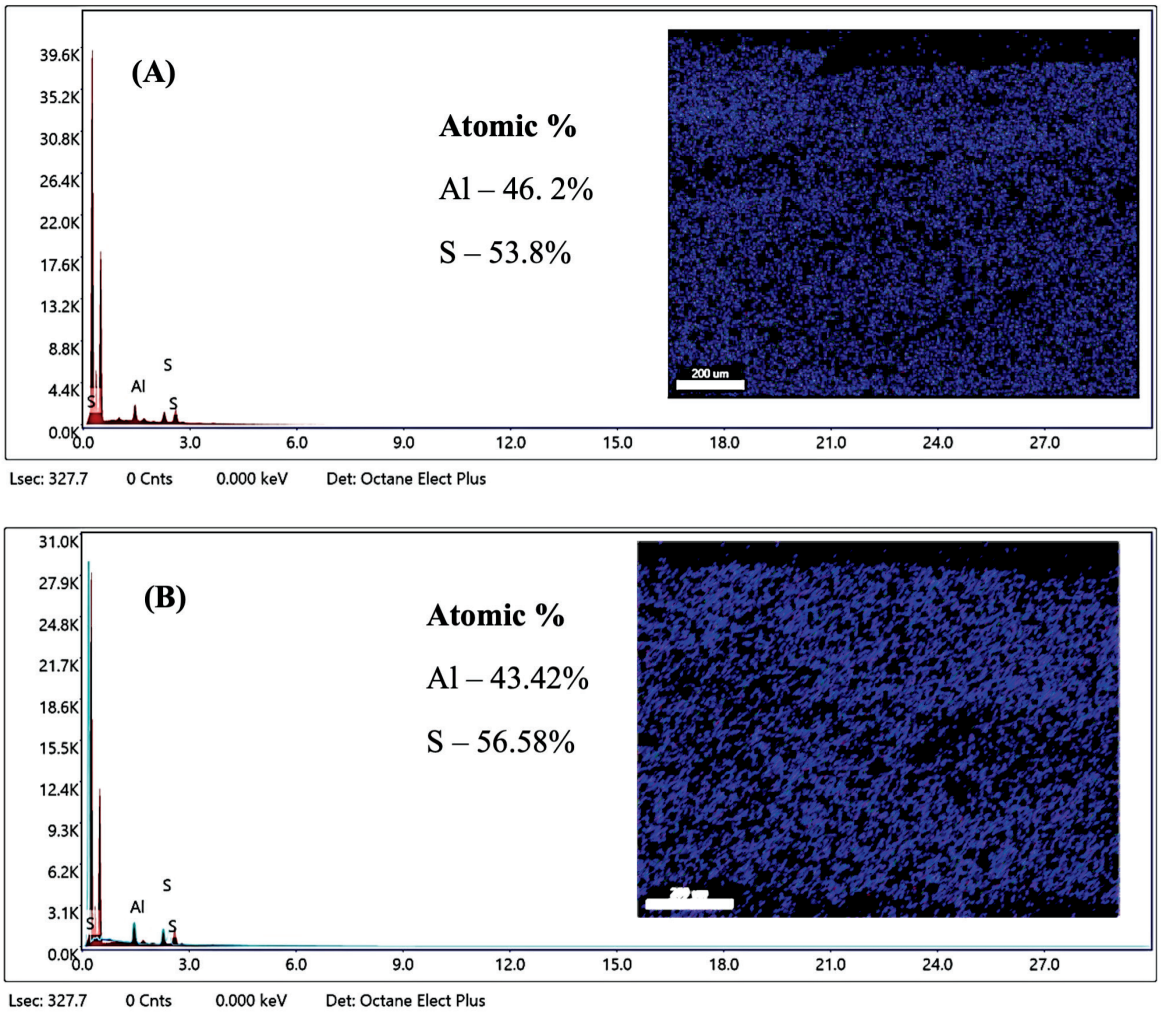

Figure 6. Elemental mapping of crust leather:
Cross-sectional view **(a)** without syntan and **(b)** with syntan

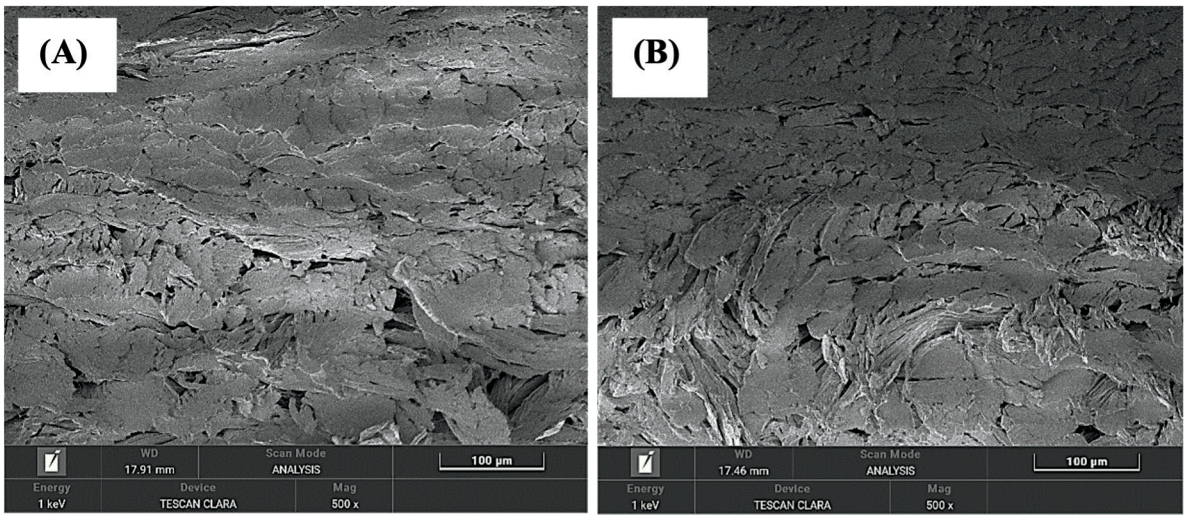

Figure 7. Cross-sectional view **(a)** without syntan and **(b)** with syntan

Conclusions

A practically viable salt-free aluminium tanning has been developed by changing the order of addition of masking salt (i.e) the addition of masking salt before the acidification process to increase the electrolyte concentration in the system. Further, it was optimized that the addition of 3% sodium carbonate (based on the weight of aluminum sulfate) along with aluminium sulfate neutralizes the acidity without affecting its tanning performance. The addition of 1.5% Al_2O_3, 5% phenolic syntan, and Al to citrate ratio of 1:0.2 was found to be an optimal condition for high-performance tanning. Further, the synergetic effect of aluminium and phenolic syntan increased the shrinkage temperature by 6°C and lowered the rate of shrinkage by 74% when compared to leather produced without syntan. However, no considerable differences have been observed for aluminium exhaustion and aluminium leaching. The order of addition of phenolic syntan and its effect on tanning performance is negligible, however, it improves the mechanical properties and fiber compactness. SEM-EDAX study indicates that the aluminium was uniformly distributed throughout the cross-section. Hence, the developed chrome-free tanning system is easy to practice with environmental/economic benefits.

Acknowledgement

The authors thank the Council of Scientific and Industrial Research (CSIR), India for financial support (OLP-2319) and the CSIR-CLRI-CATERS division for SEX-EDAX analysis. CSIR-CLRI's Communication Number 1947.

Conflict of Interest

Authors declare that no conflict of interest exists.

References

1. Palop, R and Agustín, M.; Auxiliary agents with non-swelling capacity used in pickling/tanning processes. Part I. *JSLTC* **86**, 139-142, 2002.
2. Agustín, M., Rius, A., Cot, J., Lalueza, R and Palop, R.; Salinity reduction in the production of nappa skins by using agents with non-swelling capacity in pickling/tanning. *JSLTC* **89**, 2005.
3. Legesse, W., Thanikaivelan, P., Rao, J.R and Nair, B.U.; Underlying principles in chrome tanning:part 1. Conceptual designing of pickle-less tanning. *JALCA* **97**, 82-94, 2002.
4. Thanikaivelan, P., Rao, J.R., Nair, B.U and Ramasami, T.; Underlying principles in chrome tanning: Part 2. Underpinning mechanism in pickle-less tanning. *JALCA* **99**, 82-94, 2004.
5. Aravindhan, R., Saravanabhavan, S., Rao, J.R and Nair, B.U.; A bio-driven lime and pickle free tanning way for greener garment leather production. *JALCA* **99**, 53-66, 2004.
6. Saravanabhavan, S., Aravindhan, R., Thanikaivelan, P., Rao, J.R and Nair, B.U.; Green solution for tannery pollution: effect of enzyme based lime-free unhairing and fibre opening in combination with pickle-free chrome tanning. *Green Chem.* **5**, 707-714, 2003.
7. Sathish, M, Aravindhan, R, and Raghava Rao, J; Salt-free chromium tanning: Practical approaches. *JALCA*, 117, 3-8, 2022
8. Patent No PCT/NL2020/050773, Zeolite composition suitable for tanning
9. Xinhua, L, Youyou, W, Xuechuan, W, Tengfei, H, Wanni, W and Huie, J; A salt-free pickling and chrome-free tanning technology: a sustainable approach for cleaner leather manufacturing, *Green Chemistry*, 24, 2179-2192, 2022.
10. Madhan, B, Afreen, F and Nair, B.U; Tanning agent based on mixed metal complexes of aluminium and zinc, *JALCA*, 96, 343-349, 2001.
11. Patent No. CN102787181A, Zirconium-aluminum-titanium complex tanning agent based less-chrome tanning method.
12. Chandra babu, N.K, Karthikeyan, R, Ramesh, R, Usha, R and Ramasami, T; New perspectives in iron tanning (https://www.semanticscholar.org/paper/NEW-PERSPECTIVES-IN-IRON-TANNING-Babu Karthikeyan/8031efb422a691252eb626aae20331b51e10aef4) - Accessed on October 2023

13. Fathima, N, Chandrabose, M, Aravindhan, R, Raghava Rao, J and Nair, B.U; Iron-phosphonium combination tanning: Towards a win-win approach, *JALCA*, 100, 273-281, 2005.
14. Zhicheng, J, Mi, G, Javier, R, Wei, D, Changwei, H and Bi shi; On the development of chrome-free tanning agents: An Advanced Trojan Horse Strategy using 'Al-Zr-Oligosaccharides' produced by the depolymerization and oxidation of biomass, *Green Chemistry,* 23, 1-12, 2021.
15. US Patent No 7169191, Process for preparing a synthetic aluminium tanning agent.
16. Patent No CN115011742, Epoxy modified collagen polypeptide-based organic chromium-free tanning agent, preparation method and application
17. IUP 6.; Measurement of tensile strength and percentage elongation. *JSLTC* **84**, 317-321, 2000.
18. IUP 8.; Measurement of tear load- Double edge tear. *JSLTC* **84**, 327-329, 2000.
19. SLP9, Measurement of distension and strength of grain by the ball burst test, *JSLTC*,1996.
20. IUP 2.; Sampling. *JSLTC* **84**, 303-308, 2000.


GreenTan®
Eco-friendly leather tanning system for our greener future.
GREENTAN
GreenTan® C
GreenTan® M-5
GreenTan® N-90
GreenTan® T-22M
Tel: (603) 772-3741 • www.CHEMTAN.com

Lifelines

Md. Abdur Razzaq, a senior scientific officer at the Leather Research Institute (LRI), BCSIR, Bangladesh. He completed a bachelor's degree in leather engineering from the University of Dhaka and Master's in applied chemistry from the Islamic University in 2011 and 2017, respectively. Now he is engaged in R&D projects focusing on wastewater parameters and working on different steps of leather processing like salt-reduced or free preservation techniques, ammonia-reduced or free deliming, Eco-friendly tanning or retanning, Eco-friendly dyeing of leather, Eco-friendly fat liquoring of leather, etc.

Md. Motinur Rahman is presently a scientific officer at Institute of Electronics, Bangladesh Atomic Energy Commission. He received a M.Sc. degree in Electrical and Electronic Engineering from University of Dhaka in 2017.

M. Mahfuzur Rahman is a principle scientific officer of Bangladesh Atomic Energy Commission (BAEC). He did graduate and post-graduate work in the Department of Chemistry under the National University and Bangladesh University of Engineering and Technology (BUET) respectively. His research interests are Design, Fabrication and Characterization of Radiation Shielding Composite Materials and the Study of Structural Morphology and Elemental Analysis of the Fabricated Radiation.

Md. Salamat Ullah is working in foreign trade of Rupali Bank Limited, Bangladesh. He graduated from the University of Dhaka, Dhaka, Bangladesh from the Department of Leather Product Engineering.

Qixin Han is currently a Master's student at the School of Information Science and Engineering, Shandong Normal University, Jinan, China. His research interests include damage detection and image analysis.

Yushan Wan is currently a student at the School of Information Science and Engineering, Shandong Normal University, Jinan, China. His research interests include machine learning and image analysis.

Luwen Cao is currently a Master's student at the School of Information Science and Engineering, Shandong Normal University, Jinan, China. His research interests include damage detection and image analysis.

Rong Luo is currently an Associate Professor at the State Key Laboratory of Biobased Materials and Green Papermaking, Qilu University of Technology (Shandong Academy of Science), Jinan, China. Her research interests include functional polymer materials and coating materials.

Yafei Sun is currently a Master's student at the State Key Laboratory of Biobased Materials and Green Papermaking, Qilu University of Technology (Shandong Academy of Science), Jinan, China. His research interests include functional polymer materials, coating materials.

Jia Weikuan is currently an associate professor at the School of Information Science and Engineering, Shandong Normal University, Jinan, China. His research interests include artificial intelligence, agricultural automation, and machine learning.

Chao Lei, see *JALCA* **118**, 134, 2023

Weixing Xu is currently an Associate Research Fellow in National Engineering Laboratory for Clean Technology of Leather Manufacture, Sichuan University. He received his Ph.D. degree in Biomass Chemistry and Engineering at Sichuan University in 2017. He joined Sichuan University as a research assistant from 2017 to 2022. His research focuses on biomass / polymer composite material.

Bi Shi, see *JALCA* **99**, 220, 2004

Yunhang Zeng, see *JALCA* **118**, 134, 2023

M. Sathish has obtained his Ph.D in Leather Technology and is currently working as a Scientist, at CSIR-CLRI, Regional Centre, Kolkata. His area of interest on the development of low-water and chemical economy-based leather processing.

Surojit Manna is a M.Tech student of the Government of College of Engineering and Leather Technology, Kolkata

Nakkala Gopi Krishna is working as a Technical Assistant at CSIR-CLRI Regional Centre, Kolkata.

Excellent – Bisphenol optimized syntans to achieve high leather quality

Through dedicated research we have developed a core range of bisphenol optimized syntans.
The first, TANIGAN® MBO Liq, TANIGAN® OSO Liq and TANIGAN® FAO Liq, have already been launched.
These TFL pioneering syntans address the latest regulatory challenges ahead of time with a BPS content below detection limit and are completely free of BPF. These remain an essential part of Wet-end processing ensuring the required leather tightness, fullness, softness and fastness attained.
They also consume less energy in their production and have a lower carbon dioxide footprint.
You can expect further product launches adding onto these essential "building blocks" shortly.

TFL – Great chemicals. Excellent advice.

» www.tfl.com

Chemtan waterproof technology – inspired by nature

CHEMTAN

Tel: (603) 772-3741
www.CHEMTAN.com